nature metabolism

Article

https://doi.org/10.1038/s42255-025-01243-8

Glycogen drives tumour initiation and progression in lung adenocarcinoma

Received: 29 November 2024

Accepted: 12 February 2025

Published online: 11 March 2025

Check for updates

Harrison A. Clarke[1,2,13], Tara R. Hawkinson[1,2,13], Cameron J. Shedlock[1,2], Terrymar Medina[1,2], Roberto A. Ribas[1,2], Lei Wu[1,2], Zizhen Liu[1,2,3], Xin Ma[1,4], Yi Xia[4], Yu Huang[5,6,7], Xing He[5,6,7], Josephine E. Chang[8], Lyndsay E. A. Young[9,10], Jelena A. Juras[8], Michael D. Buoncristiani[8], Alexis N. James[8], Anna Rushin[1], Matthew E. Merritt[1], Annette Mestas[1], Jessica F. Lamb[8], Elena C. Manauis[10], Grant L. Austin[10], Li Chen[4], Pankaj K. Singh[1,2], Jiang Bian[5,6,7], Craig W. Vander Kooi[1,2], B. Mark Evers[9], Christine F. Brainson[9,11], Derek B. Allison[9,12], Matthew S. Gentry[1,2,14] ✉ & Ramon C. Sun[1,2,3,14] ✉

Lung adenocarcinoma (LUAD) is an aggressive cancer defined by oncogenic drivers and metabolic reprogramming. Here we leverage next-generation spatial screens to identify glycogen as a critical and previously underexplored oncogenic metabolite. High-throughput spatial analysis of human LUAD samples revealed that glycogen accumulation correlates with increased tumour grade and poor survival. Furthermore, we assessed the effect of increasing glycogen levels on LUAD via dietary intervention or via a genetic model. Approaches that increased glycogen levels provided compelling evidence that elevated glycogen substantially accelerates tumour progression, driving the formation of higher-grade tumours, while the genetic ablation of glycogen synthase effectively suppressed tumour growth. To further establish the connection between glycogen and cellular metabolism, we developed a multiplexed spatial technique to simultaneously assess glycogen and cellular metabolites, uncovering a direct relationship between glycogen levels and elevated central carbon metabolites essential for tumour growth. Our findings support the conclusion that glycogen accumulation drives LUAD cancer progression and provide a framework for integrating spatial metabolomics with translational models to uncover metabolic drivers of cancer.

Lung adenocarcinoma (LUAD) represents a highly aggressive and lethal subtype of lung cancer[1]. Despite advances in treatment, the prognosis for patients with LUAD remains poor[2], as the disease is often diagnosed with advanced tumours[3], limiting the effectiveness of existing therapeutic options[4,5]. An intense area of research emphasizes the complex spatial and microenvironmental metabolic alterations that support tumour growth and survival in LUAD. Cancer cells, including those in LUAD, reprogram their metabolism to meet the increased demands for energy and biosynthetic precursors[6], facilitating rapid proliferation[7], and resistance to stress[8]. These metabolic adaptations are influenced by multiple factors, including local and microenvironmental nutrient availability[9] and specific signalling pathways that can drive oncogenesis[10,11]. The continuing evolving landscape of cancer metabolism, particularly in aggressive subtypes such as LUAD, presents promising avenues for the development of future prevention and treatment strategies.

Cancer metabolism, characterized by alterations in the metabolic pathways within tumour cells[12,13], is an area that has been the focus of

A full list of affiliations appears at the end of the paper. ✉e-mail: matthew.gentry@ufl.edu; ramonsun@ufl.edu

intense research[14,15]. Although central to metabolism, the direct role of glycogen in cancer metabolism has been less explored. Historically, studying glycogen metabolism has been challenging due to its complex biochemical properties and the difficulties in detecting and quantifying glycogen in a tissue-specific context[16]. However, recent advances in mass spectrometry imaging (MSI) have dramatically enhanced our ability to assess glycogen and its metabolism within the tissue microenvironment[16,17]. Although glycogen is not traditionally classified as an oncometabolite, increasing evidence suggests that glycogen accumulation is pathogenic in lung, liver and ovarian cancers[18,19]. In lung cancer, nuclear glycogen serves as a carbon source for acetyl groups involved in regulating histone acetylation, a critical process in modulating gene expression[20]. In liver cancers, glycogen liquid–liquid phase separation can lead to Hippo signalling inhibition and increased tumour incidence[21]. Furthermore, glycogen has been reported to foster tumourigenesis in ovarian cancer by acting as a reservoir metabolite that is channelled between tumour and stromal cells, facilitating the exchange of nutrients and metabolites that favour tumour growth and progression[22]. These findings highlight the complex and multifaceted roles of glycogen in cancer metabolism that warrant further exploration in the context of tumour initiation and progression.

Spatial biology is revolutionizing our ability to understand the microenvironmental phenotypes and phenotypes of diseases, providing insights into how spatially organized molecular interactions give rise to cellular neighbourhoods[23]. One rising application of spatial biology is spatial metabolomics, which utilizes advanced imaging to achieve single-cell, spatially resolved metabolic phenotypes[24,25]. Matrix-assisted laser desorption/ionization (MALDI) imaging has been applied to the visualization of metabolic landscapes in situ, capturing the heterogeneity and complexity of metabolic reprogramming within tumours[26]. Recent advancements have expanded MALDI imaging capabilities to include single-cell metabolomics[16,27] and isotopic tracing[28], making it possible to adapt this powerful technology to dissect biomolecular mechanisms driving disease processes with remarkable results[16,29]. In this study, we used advanced spatial metabolomics techniques to investigate metabolic heterogeneity in a cohort of patients with non-small-cell lung cancer (NSCLC). Our findings identified glycogen as a critical metabolite specifically in patients with LUAD. Subsequent analysis demonstrated that increased glycogen promotes accelerated tumour progression in a LUAD mouse model. Conversely, a genetic mouse model that cannot synthesize glycogen failed to form mature tumours in the same mouse cancer model, further confirming the role of glycogen metabolism in LUAD. By integrating human specimen analysis with genetically modified models, we underscore the utility of spatial metabolomics in identifying key metabolic vulnerabilities, ultimately informing disease aetiologies and advancing our understanding of tumour metabolism.

Results

Glycogen is a hallmark of LUAD tumours

Glycogen is challenging to study owing to its biophysical and biochemical properties. To overcome this challenge, we developed a robust and sensitive method to study spatial glycogen tissue heterogeneity by MALDI imaging[16]. To establish this method for translational research in lung cancer, we first confirmed the spatial distribution of glycogen between adjacently cut tissue sections using a classical immunohistochemical method with an anti-glycogen antibody[20,30–34] (Extended Data Fig. 1). Both methods displayed similar glycogen distribution patterns in human lung tumours (Extended Data Fig. 1). Using the MALDI imaging method for quantifying the spatial distribution of glycogen and glycogen architecture (that is, glucose chain length) in tissue sections (Extended Data Fig. 2a,b and Supplementary Fig. 1), we analysed a tissue microarray (TMA) of NSCLC tumour samples from a cohort of patients with lung cancer (Fig. 1a–c and Extended Data Fig. 2b). We observed substantial heterogeneity in the amount of glycogen across patients with lung cancer. To ascertain if the differences were related to the subtype of lung cancer, we compared glycogen abundance in LUAD and lung squamous cell carcinoma (LUSC) samples. LUAD patient samples displayed substantially more glycogen than LUSC patient samples (Fig. 1b,d), particularly with respect to chain lengths 6–9 (Fig. 1c). Furthermore, glycogen architecture was shifted towards aberrant glycogen with longer chain lengths in the LUAD samples (Fig. 1c). Thus, glycogen accumulation was increased in LUAD patient samples, and the architecture of the glycogen differed in LUAD compared with LUSC tumour tissue. Spatial analysis revealed that the glycogen accumulates uniquely in the tumour regions rather than in the stromal or vascular regions (Fig. 1d,e). Finally, we performed absolute glycogen quantitation in patient tissue sections and determined that the amount of glycogen is 0.3–1.5 ng per pixel in LUAD compared with 0.04 ng per pixel in LUSC (Extended Data Fig. 3 and Supplementary Figs. 2 and 3).

We then examined the relationship between glycogen and cancer grade in an expanded cohort of patients with LUAD ($n = 276$). We observed that increasing levels of glycogen correlate with a more advanced grade of LUAD tumours, that is, higher glycogen in poorly differentiated LUAD cases (Extended Data Fig. 4a,b). In addition, survival analyses demonstrated that patients with LUAD with higher glycogen content in their tumours exhibited shorter survival and worse prognosis. This result is indicated by the separation of glycogen levels by both medium as well as quartiles (Extended Data Fig. 4c). To further assess whether glycogen is a good predictor of patient survival, we performed area under the receiver operating characteristic (AUROC) and area under the precision-recall curve (AUPOC) analyses with a machine-learning algorithm (random forest model) in our patient cohort. Glycogen predicted LUAD death with an AUROC score of 0.846 and AUPRC score of 0.888 (Extended Data Fig. 4d). Collectively, these data highlight that glycogen is an excellent prognostic factor of LUAD and warrants additional molecular investigation into its role in tumour progression.

To determine whether specific driver mutations were associated with glycogen accumulation, we analysed glycogen in human LUAD tumours with loss-of-function mutations in KRAS-only (K), EGFR-only (E), KRAS/p53 (KP), KRAS/LKB1 (KL), KRAS/LKB1/p53 (KPL) and KRAS/KEAP/LKB1 (KKL). Compared with glycogen abundance in normal lung tissue or in LUSC samples, LUAD samples with any tested driver mutation(s) exhibited increased glycogen (Fig. 1f,g). However, the glycogen-rich phenotype is not unique to a specific mutation or combination of mutations. Glycogen accumulation also occurred in mouse genetic models (K, KP, KL and E) of these lung cancers (Extended Data Fig. 2c,d). These results suggest that the increased glycogen in LUAD compared with LUSC is characteristic of the subtype of lung cancer and not due to a genetically defined subset of LUAD samples. Furthermore, the consistency between the mouse and human tumours established the validity of using these mouse models to study this glycogen phenomenon.

Based on promising clinical observations demonstrating that increased glycogen correlates with higher tumour grade and worse prognosis in patients with LUAD, we hypothesized that elevated glycogen levels actively promote tumour progression. To test this hypothesis, we utilized two distinct approaches to increase lung glycogen content in the inducible $Kras^{G12D}$ and knockout of *Tp53* (LSL-$Kras^{G12D}$/$p53^{fl/fl}$; KP) mouse model of LUAD. The first approach involved increased lung glycogen through dietary challenge, and the second approach used a genetic model that predisposes to glycogen accumulation, both creating a high-glycogen phenotype directly in lung tissues.

Higher glycogen promotes increased tumour progression

Both carbohydrates and fats have been shown to impact liver glycogen metabolism[35,36]. Given the unique metabolic environment of the lung compared with the liver, we systematically tested different dietary

https://doi.org/10.1038/s42255-025-01243-8

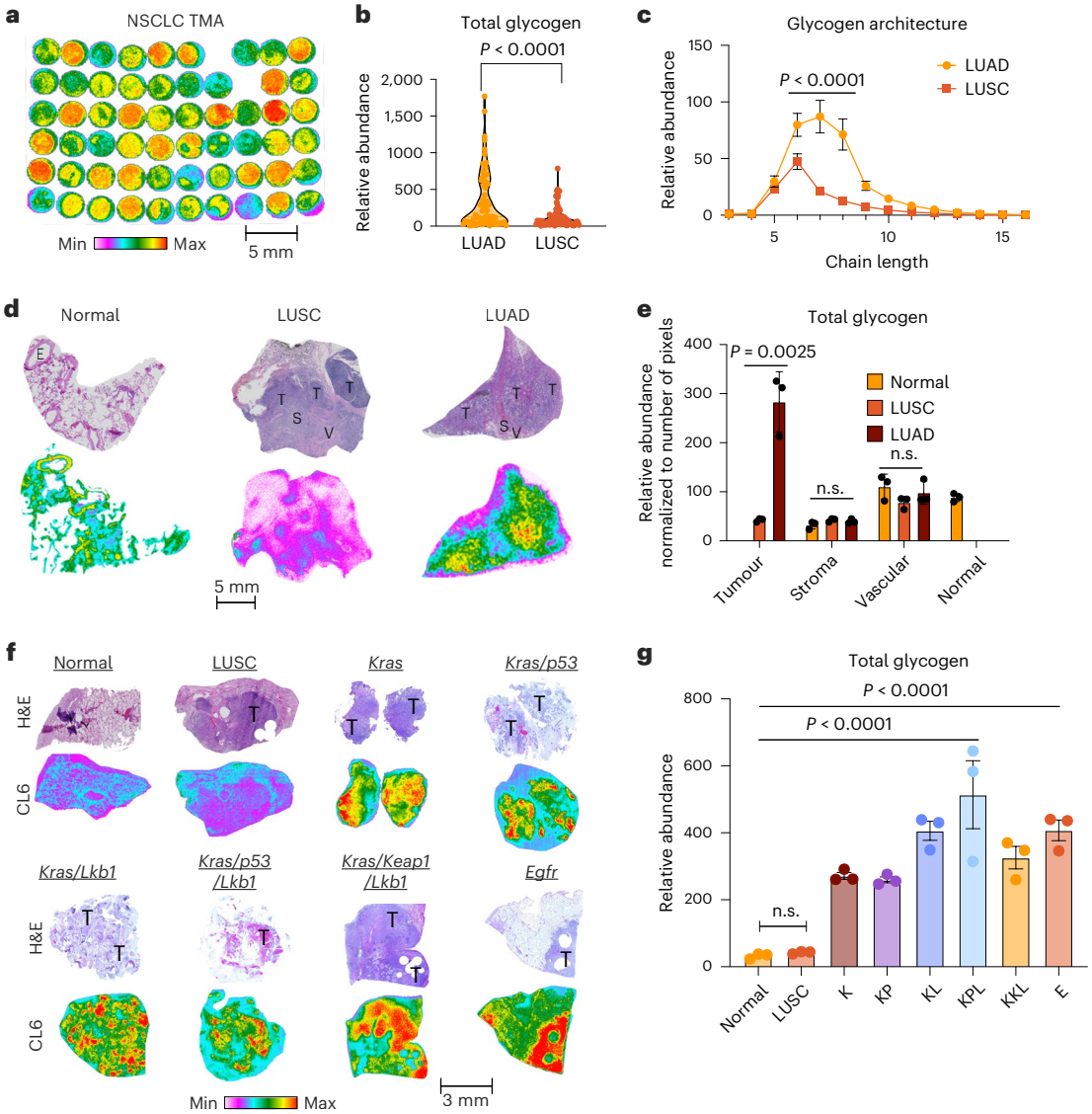

Fig. 1 | Intratumoural glycogen uniquely accumulates in LUAD. **a**, Representative heatmap of MALDI glycogen imaging in a TMA format. **b**, Relative glycogen abundance correlating to glucose polymer 7 between LUAD ($n = 77$ patients) and LUSC ($n = 68$ patients) extracted from MALDI spatial glycogen analysis from the lung cancer TMA shown in **a** (P value indicated, two-tailed t-test). **c**, Glycogen chain length analysis between LUAD ($n = 77$) and LUSC ($n = 68$) showing the greatest difference between chain lengths 6 and 9 (mean ± s.e.m., P value indicated, two-way ANOVA and Šidák's multiple-comparison test). **d**, Representative spatial glycogen analysis in normal lung, LUSC and LUAD tumours. Corresponding haematoxylin and eosin (H&E) images of each tumour are shown above the MALDI heatmap image of glycogen. T, tumour; S, stromal; V, vascular. **e**, Relative glycogen abundance between normal, LUAD and LUSC subregions such as tumour, stroma and endothelial lining extracted from MALDI spatial glycogen analysis in **d** (mean ± s.e.m., P value indicated, two-way ANOVA). $n = 3$ (average of 3 regions of interest of 500 pixels within each region). **f**, Representative spatial glycogen analysis in LUAD tumours with different driver mutations. LUSC and normal lung are used for control. Corresponding H&E images of each tumour are shown above the MALDI heatmap image of glycogen chain length 6 (CL6) in human patient biopsies. Loss-of-function mutations: KRAS-only (K), KRAS/p53 (KP), KRAS/LKB1 (KL), KRAS/LKB1/p53 (KPL), KRAS/KEAP/LKB1 (KKL) and EGFR-only (E). **g**, Relative glycogen abundance from human patient LUAD tumours with different driver mutations shown in **f**. LUSC and normal lung are used for control ($n = 3$ individual patients; mean ± s.e.m., P values indicated, one-way ANOVA adjusted for Dunnett's multiple comparison). n.s., not significant.

compositions to identify the optimal strategy that would drive glycogen accumulation specifically in the lungs of mice. First, wild-type mice were administered vehicle control (H_2O), high-fructose corn syrup (HFCS, a refined carbohydrate)[37,38], corn oil (a fat)[39,40] or a combination of HFCS and corn oil (HFCS + corn oil, calorie matched) by oral gavage to ensure consistent intake of these dietary components (Extended Data Fig. 5a). After 2 weeks (14 days), mice receiving the combination diet (that is HFCS + corn oil) exhibited dramatically increased glycogen levels in their lungs compared with mice receiving vehicle or the HFCS or corn oil alone (Extended Data Fig. 5a,b). Furthermore, mice on the combination diet exhibited increases in glycogen chain lengths 5–10 in their lungs compared with mice on HFCS or corn oil alone (Extended Data Fig. 5b). Comparable levels of lung glycogen were observed between HFCS or corn oil alone and vehicle (Extended Data Fig. 5a,b). Importantly, none of the diets administrated by oral gavage triggered changes in glucose intolerance or body weight during the 14 days (Extended Data Fig. 5c–f). However, each diet except the vehicle control triggered glycogen accumulation in the liver, with the HFCS cohort and the combination cohort displaying higher levels than the corn oil cohort (Extended Data Fig. 5g,h). This tissue difference between lung and liver suggests that the lung responds differently to diets with high fat and high carbohydrate than the liver.

Next, we examined whether the combination diet increased prevalence of lung cancer. We administered either water (vehicle) or the combination (HFCS + corn oil) daily for 2 weeks to KP animals (Fig. 2a and Supplementary Fig. 4). Lung tumourigenesis was initiated following intranasal delivery of Adeno-Cre virus after dietary gavage treatment to reduce confounding effects of oral gavage. We did not continue the gavage treatment for the course of tumourigenesis to (1) perform a focused assessment on the impact of glycogen on early tumourigenesis and (2) to avoid confounding effects of gavage and stress on tumour progression[41,42]. After 100 days, mice administered the combination diet developed more tumours, and the tumours were larger than those that developed in the mice receiving water (Fig. 2b,c). Spatial glycogen analysis identified higher glycogen accumulation uniquely in the tumours of KP mice with diet treatment (Fig. 2c,d and Extended Data Fig. 5i). Furthermore, histological assessment found that an increased number of higher-grade tumours developed in KP mice receiving the combination diet (Fig. 2e). The results indicate that increased glycogen accumulation in the lung accelerated early tumourigenesis, leading to the development of more advanced tumours at the experimental endpoint.

Glycogen phosphorylation accelerates lung tumourigenesis

To further test our findings from the dietary model, we utilized a genetic model to assess the impact of high glycogen on tumour development. First, we examined the impact of glycogen metabolic enzymes on lung tumourigeneses. We performed immunohistochemistry (IHC) in the TMA cohort to analyse protein abundance of enzymes involved in glycogen synthesis and metabolism. We found that the glycogen phosphatase laforin (encoded by *EPM2A*) is markedly reduced in LUAD compared with LUSC, whereas glycogen synthase 1 (GYS1) and glycogen phosphorylase are similar (Fig. 2f and Extended Data Fig. 6a). Glycogen phosphorylation impacts glycogen utilization through cytoplasmic or lysosomal glycogen degradation routes[29]. Laforin is the glycogen phosphatase that regulates glycogen phosphate levels[43]. Using the same The Cancer Genome Atlas (TCGA) data, we found that low *EPM2A* expression was associated with worse survival in LUAD, whereas there was no significant difference in survival between patients with LUSC with high or low expression of *EPM2A* (Supplementary Data Fig. 4d). Using MALDI glycogen imaging of the cohorts, we determined that the average glycogen phosphate level was higher in LUAD patient samples than LUSC patient samples with notable increases in phosphorylated glycogen of chain lengths 6–9 in the LUAD samples (Fig. 2g and Extended Data Fig. 6b).

On the basis of the protein abundance and functional data from human patients, laforin (*Emp2a*) knockout mice (LKO) were used to examine if altered glycogen utilization and glycogen accumulation contributed to oncogenesis. Strikingly, by 4 months of age, the LKO mice exhibited increased glycogen across several chain lengths within the lung (Extended Data Fig. 6c). To determine whether the difference in glycogen abundance directly contributes to proliferative potentials, we isolated bronchiolar stem cells from both wild-type mice and LKO mice and differentiated the cells into bronchiolar and alveolar organoids[44] (Extended Data Fig. 7a). Both the number of organoid colonies and the sizes of the colonies were larger when formed from LKO cells than wild-type cells (Extended Data Fig. 7b,c), suggesting that loss of laforin activity and glycogen accumulation drive cellular proliferation even in non-transformed cells. Building on these data, we bred LKO mice with the KP mouse model to study the role of glycogen in tumourigenesis. We compared tumourigenesis and tumour growth in KP mice and KP mice crossed with LKO mice (KPL) after intranasal delivery of Adeno-Cre to activate oncogenesis in the lung only (Fig. 2h). Both mice developed lung tumours (Fig. 2i), but the tumours were both larger and more numerous in the KP/LKO mice than in the KP mice (Fig. 2i,j). As predicted, the KPL tumours exhibited more glycogen accumulation (Extended Data Fig. 7d). Histological examination also confirmed increasing percentage of higher-grade tumours in the KPL cohort similar to those observed in the KP animals administered combination diet (Extended Data Fig. 7e). Collectively, both diet gavage and the KPL models support they finding that higher glycogen leads to accelerated tumour progression.

Suppressing glycogen synthesis blunts lung tumourigenesis

Human LUAD and KP mouse models exhibit a glycogen-rich phenotype before diet or genetic challenge, suggesting active glycogen synthesis de novo. Therefore, we further investigated whether impairing glycogen synthesis could blunt tumourigenesis in the KP animal model. To test this, we crossed the Gys1$^{fl/fl}$ mouse model with the KP mouse model to generate the KP/Gys$^{fl/fl}$ (KPG) mouse model (Fig. 3a and Supplementary Fig. 5b). GYS1 is the predominate glycogen synthase isoform in peripheral tissues other than the liver[45]. In this mouse model, intranasal delivery of Adeno-Cre was used to trigger oncogenesis while simultaneously silencing Gys1 gene expression and glycogen synthesis. Both KP and KPG mice were administered intranasal delivery of Adeno-Cre, and lung tumourigenesis was allowed to occur over 100 days (Fig. 3a). At the midpoint, ~day 50, as well as ~day 95, blunted tumourigenesis was already obvious in the KPG animals compared with the KP cohorts assessed by non-invasive 7 T magnetic resonance imaging (Supplementary Fig. 5). At the endpoint, GYS1 was undetectable in the tumours of KPG mice (Supplementary Fig. 5b). Assessment by haematoxylin and eosin staining at the experimental endpoint showed that the KPG cohort had dramatically reduced tumour sizes and volumes compared with the KP group (Fig. 3b,c and Extended Data Fig. 7f,g); furthermore, histological examination showed that the KPG cohorts exhibited much lower-grade tumours (Fig. 3d).

If the administration of combination diet drives lung tumourigenesis through glycogen accumulation in the lung (Fig. 2a), then

Fig. 2 | Higher glycogen drives accelerated tumourigenesis. a, Schematics of LSL-Kras^{G12D}/p53$^{fl/fl}$ mice undergoing daily oral gavage of vehicle or HFCS + corn oil (combination) for 2 weeks followed by Adeno-Cre introduction for tumour initiation and tumourigenesis for 14 weeks (without gavage). **b**, Average tumour size and tumour volume in vehicle or HFCS + corn oil (combination) treated mice at the experimental endpoint ($n = 6$ animals per group; mean ± s.e.m., P values indicated, two-tailed t-test). **c**, Spatial glycogen analysis of lung extracted from mice gavaged with either vehicle or HFCS + corn oil (combination) treatment before administration of Adeno-Cre. Corresponding H&E images of each lung are shown above the MALDI heatmap image of glycogen CL6. **d**, Intratumoural glycogen chain length analysis between vehicle and HFCS + corn oil (combination) treatment groups showing major differences between CL5 and CL9 ($n = 9$ animals per group; mean ± s.e.m., P values indicated, two-way ANOVA and Šidák's multiple-comparison test). **e**, The distribution of tumour grades across vehicle or HFCS + corn oil (combination) treatment groups ($n = 3$ animals per group from **b**; mean ± s.e.m., P values indicated, two-way ANOVA and Tukey's multiple-comparison test). **f**, Immunohistochemical analysis of laforin, glycogen synthase (GYS) and glycogen phosphorylase (GP) from the adjacent TMA sections used in glycogen MALDI imaging ($n = 66$ patients for LUAD, 81 for LUSC, 12 for normal; mean ± s.e.m., P values indicated, one-way ANOVA and Tukey's multiple-comparison test). **g**, Loss of laforin in LUAD corresponds to opposing increase in glycogen phosphate (phosphorylated glucose polymer 7) levels compared with LUSC measured by MALDI ($n = 66$ patients for LUAD, 77 for LUSC mean ± s.e.m., P value indicated, two-tailed t-test). **h**, Schematics of induction of tumourigenesis in LSL-Kras^{G12D}/p53$^{fl/fl}$ (KP) and LSL-Kras^{G12D}/p53$^{fl/fl}$/LKO (KPL) mice followed by tumour analysis. **i**, Representative H&E images of tumour formation from LSL-Kras^{G12D}/p53$^{fl/fl}$ (KP) and LSL-Kras^{G12D}/p53$^{fl/fl}$/LKO (KPL) mice. **j**, Average tumour size and tumour volume in LSL-Kras^{G12D}/p53$^{fl/fl}$ (KP, $n = 5$) and LSL-Kras^{G12D}/p53$^{fl/fl}$/LKO (KPL, $n = 6$) mice at the experimental endpoint (mean ± s.e.m., P values indicated, two-tailed t-test). Panels **a** and **h** created with BioRender.com.

https://doi.org/10.1038/s42255-025-01243-8

the combination treatment should not enhance tumourigenesis and tumour growth in KPG mice owing to their inability to synthesize glycogen during tumourigenesis. Therefore, we performed dietary experiments by administrating vehicle and combination diet to the KPG mice before receiving the Adeno-Cre administration (Fig. 3a). In agreement with the hypothesis, the additional combination diet did not increase tumour size in KPG mice at either day 50, day 95 or the 100-day endpoint of the experiment (Fig. 3b–d, Extended Data Fig. 7f and Supplementary Fig. 5). Glycogen MALDI imaging analysis also confirmed that KPG, KPG:vehicle and KPG:combination diet cohorts all exhibit significantly lower glycogen compared with KP mice when normalized to tumour size (number of pixels) (Fig. 3e). Collectively, data from the genetically modified mouse models and dietary treatment demonstrate that glycogen synthesis is a key metabolic requirement of LUAD tumourigenesis.

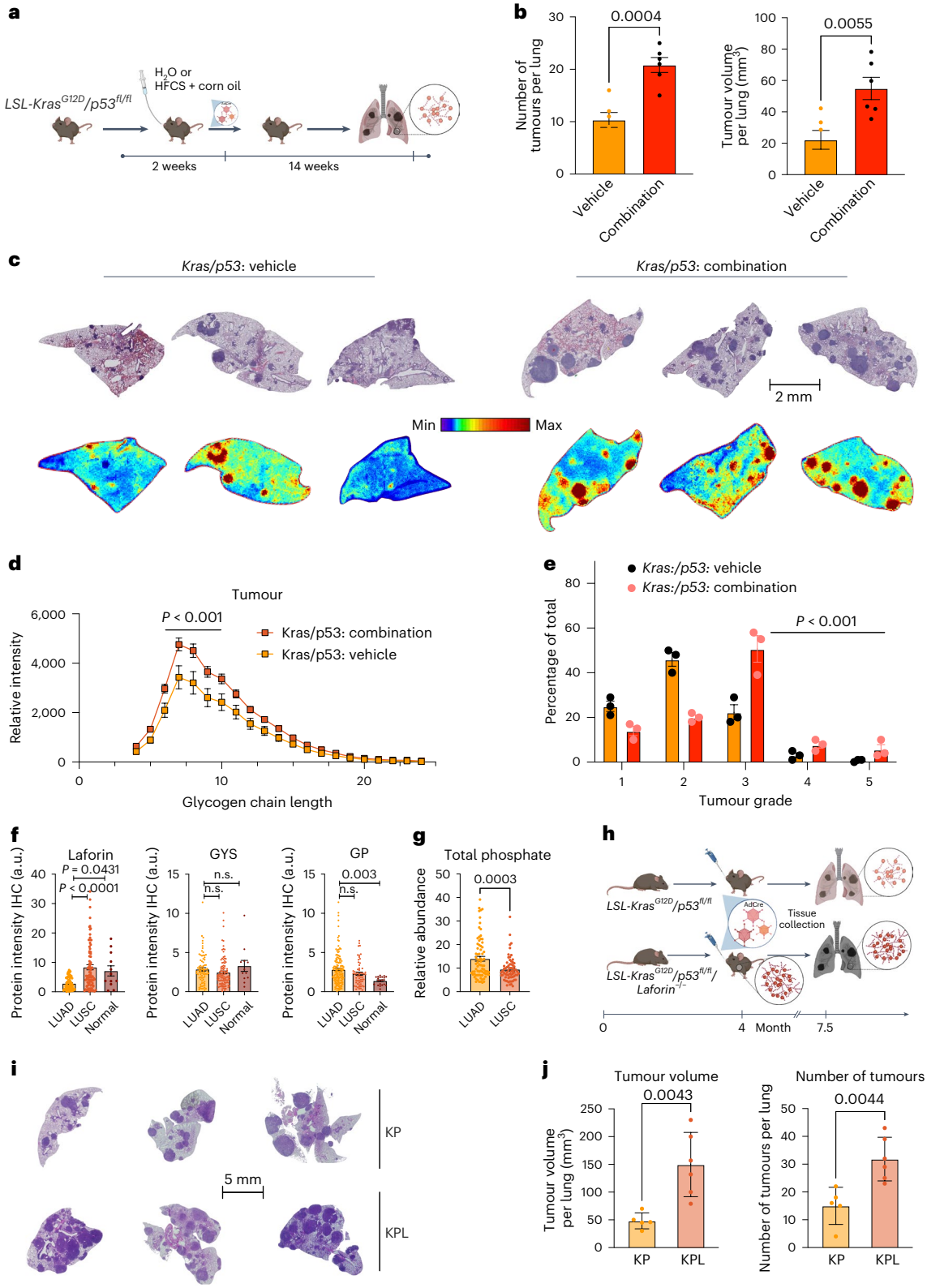

https://doi.org/10.1038/s42255-025-01243-8

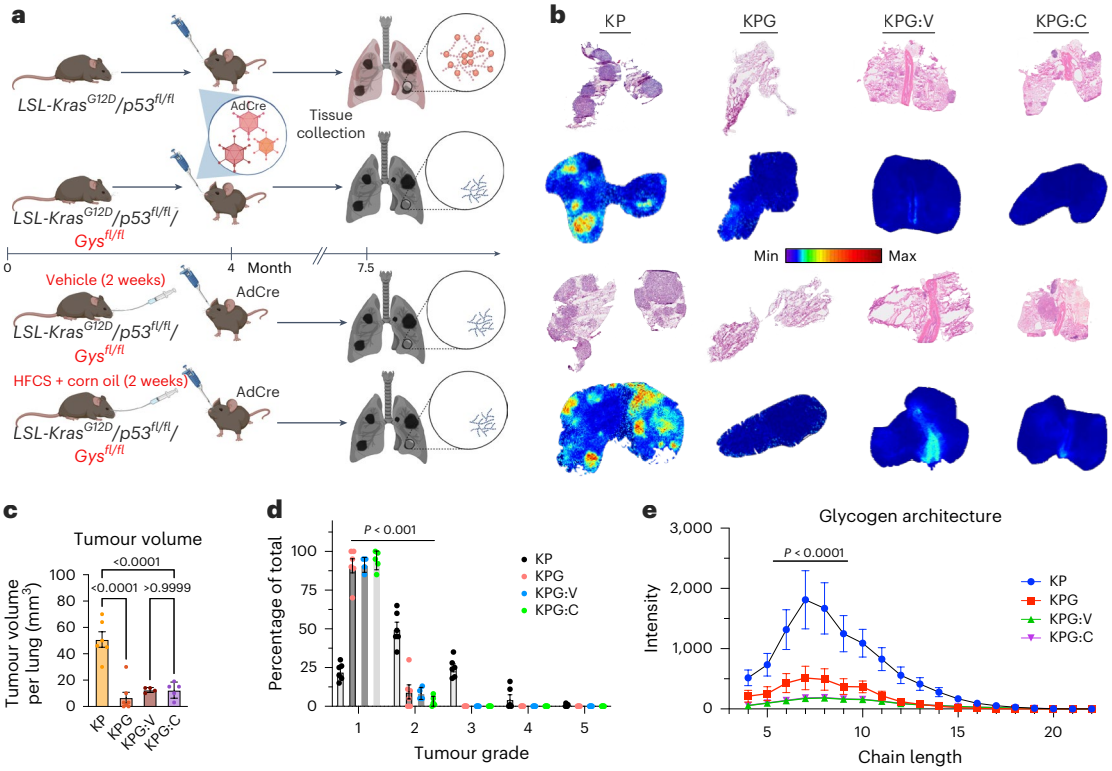

Fig. 3 | Glycogen synthesis is required for tumourigenesis. a, Schematics of induction of tumourigenesis in LSL-Kras^{G12D}/p53$^{fl/fl}$ (KP); LSL-Kras^{G12D}/p53$^{fl/fl}$/Gys$^{fl/fl}$ (KPG); LSL-Kras^{G12D}/p53$^{fl/fl}$/Gys$^{fl/fl}$ (KPG):vehicle (V); LSL-Kras^{G12D}/p53$^{fl/fl}$/Gys$^{fl/fl}$ (KPG):combination diet (C) mice followed by tumour analysis. **b**, Representative H&E images and MALDI imaging of an adjacent tissue section showing tumour formation and glycogen levels LSL-Kras^{G12D}/p53$^{fl/fl}$ (KP); LSL-Kras^{G12D}/p53$^{fl/fl}$/Gys$^{fl/fl}$ (KPG); LSL-Kras^{G12D}/p53$^{fl/fl}$/Gys$^{fl/fl}$ (KPG):vehicle; LSL-Kras^{G12D}/p53$^{fl/fl}$/Gys$^{fl/fl}$ (KPG):combination diet animals ($n = 2$ each). **c**, Average tumour size and tumour volume in all four cohorts of mice at the experimental endpoint ($n = 6$ animals for KP, 6 for KPG, 4 for KPG:V and 5 for KPG:C; mean ± s.e.m., P values indicated, one-way ANOVA and Tukey's multiple comparison). **d**, The distribution of tumour grades across all four cohorts of mice ($n = 6$ animals for KP, 6 for KPG, 4 for KPG:V and 5 for KPG:C; mean ± s.e.m., P values indicated, one-way ANOVA adjusted for Tukey's multiple comparison). **e**, Intratumoural glycogen chain length analysis for all four cohorts showing major differences between CL5 and CL9 ($n = 6$ animals for KP, 6 for KPG, 4 for KPG:V and 5 for KPG:C; mean ± s.e.m., P values indicated, two-way ANOVA adjusted for Tukey's multiple comparison). Panel **a** created with BioRender.com.

LUAD glycogen supplies substrate for cancer metabolism

Glycogen can drive tumourigenesis through signalling cascades[21] or central carbon metabolism[20]. To delineate which of the two routes was relevant in LUAD, we performed proteomic and phosphoproteomic analysis from both KP and KPL tumours (Supplementary Table 1). We did not identify significant differences between the two tumour models using either principal component analysis or analysis of volcano plots with a 1 $\log_2$(fold change) and 1 −log value cut-off (Extended Data Fig. 8a,b). These results suggest that the growth advantage of the KP/LKO tumours was not through a change in signalling pathways but, instead, through altered metabolism.

To investigate spatial correlations between metabolites and glycogen in tissue sections, we developed a multiplexed spatial technique to assess the cellular metabolome and glycogen from a single tissue section (Fig. 4a). Using this new approach, we applied quantitative spatial metabolome analysis (Fig. 4b–d, Extended Data Fig. 8c,d and Supplementary Fig. 6). We observed a positive correlation between relative glycogen abundance in the tumours of both genotypes and relative glucose, glucose-6-phosphate (G6P), citrate and adenosine diphosphate (ADP) abundance (Fig. 4c) along with many other metabolites in the central carbon metabolic pathway. Quantitative analysis of the abundance of central carbon metabolites in tumours of each genotype revealed that KPL tumours displayed notable higher pools of central carbon metabolites compared with KP alone, with glucose, citrate, G6P and ADP shown as representative metabolites (Fig. 4d and Extended Data Fig. 8c,d).

A positive correlation between glycogen and central carbon metabolites raises the hypothesis that glycogen directly supports cancer metabolism (Fig. 4e). To assess the contribution of glycogen to cellular metabolism, we performed a pulse-chase experiment[46] using ^{13}C-glucose with a modified multiplex metabolome/glycogen assay in a chamber-well format (Extended Data Fig. 9a–c). To accurately capture ^{13}C labelling in glucose chains cleaved from glycogen, we used two-dimensional ion mobility mass spectrometry that can align ions on the basis of collision cross section (CCS)[47]. Using ion mobility mass spectrometry, we identified ^{13}C-labelled glucose chain lengths with CCS (Extended Data Fig. 10a–e and Supplementary Fig. 7). We first performed a timeline experiment to define the isotopic steady state of glycogen enrichment (Extended Data Fig. 9d,e) in the A549 lung cancer cell line. Similar to m2 (number of ^{13}carbons) TCA metabolites (citric acid, glutathione (GSH), malate and glutamate) and m3 glycolytic metabolites (pyruvate, phosphoenolpyruvate, 3-phosphoglyceric acid (3PG) and lactate), nearly 40% of glycogen chain length 7 was fully labelled in 24 h (m42, 0.4 out of 1 fractional labelling), and remained steady for 48 and 72 h (Extended Data Fig. 9d,e and Supplementary Fig. 8). We then performed the pulse-chase experiment by pulsing with ^{13}C-glucose for first 24 h, then chasing with ^{12}C-glucose for 12 h (Fig. 5a,b). The contribution of ^{13}C-glycogen to downstream metabolites was defined as the difference between vehicle or acarbose treatment (Fig. 5b,c), a pan inhibitor of GP[48], amylase[49] and both the acid and neutral α-glucosidases[50]. Acarbose blocked ^{13}C-glycogen utilization during the chase phase, resulting in a 100% increase in ^{13}C-glycogen remaining after the 12-h chase compared with the vehicle control (Fig. 5d). Concurrently, in the cells exposed to acarbose, we observed significant reductions in major central carbon metabolites, such as m2

https://doi.org/10.1038/s42255-025-01243-8

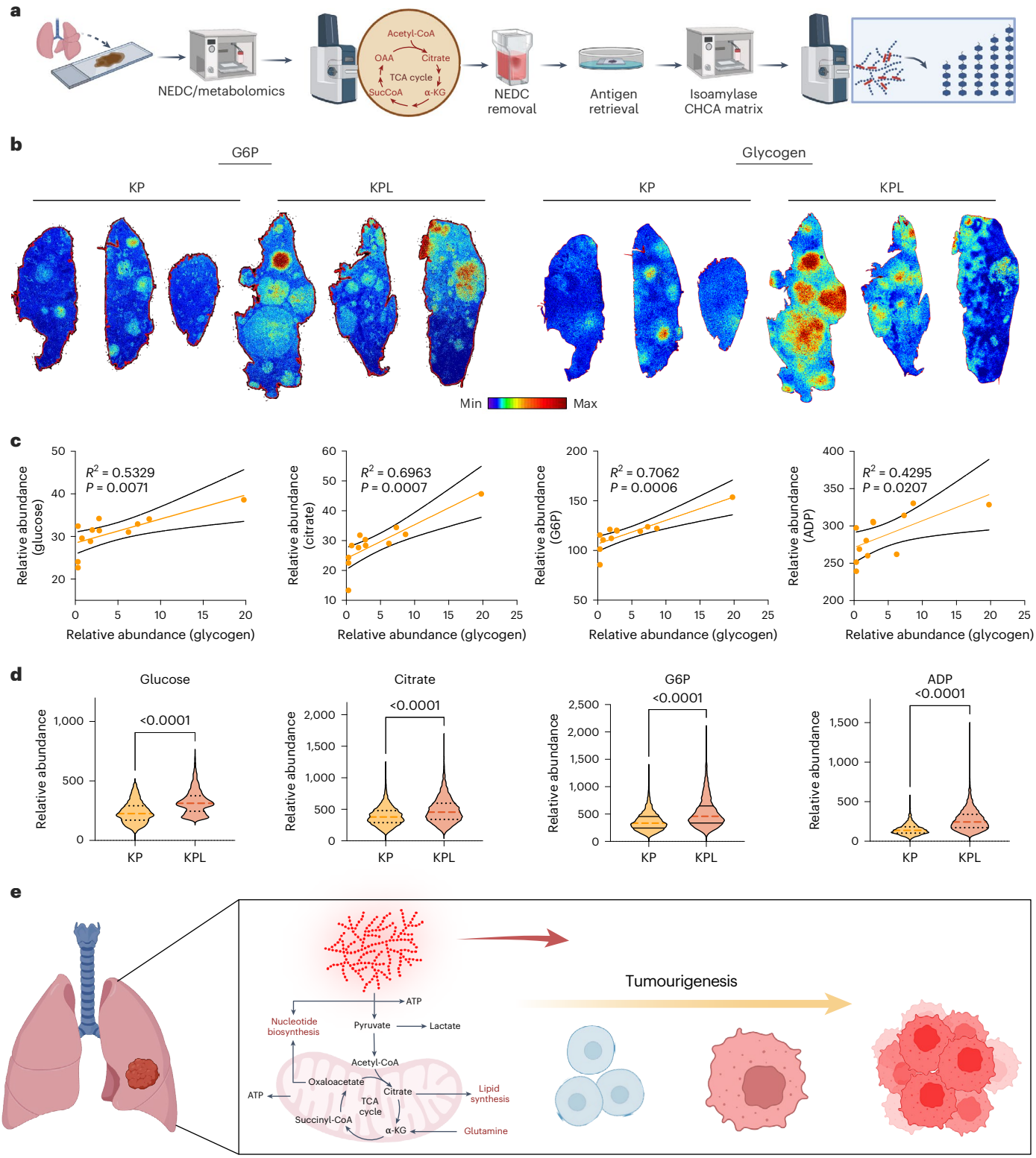

Fig. 4 | High glycogen supports metabolite pools in KP tumours. a, Schematics of a multiplexed workflow to study spatial metabolomics and spatial glycogen from a single 10-µm tissue section. NEDC, *N*-naphthylethylenediamine dihydrochloride; α-KG, α-ketoglutaric acid; OAA, oxaloacetate. **b**, A representative image of multiplexed imaging of spatial metabolomics (G6P) and glycogen in LSL-Kras^{G12D}/p53$^{fl/fl}$ (KP) and LSL-Kras^{G12D}/p53$^{fl/fl}$/LKO (KPL) tumours. Data shown are from a single experiment of three repeats. **c**, Correlative analysis of relative glycogen abundance and metabolite abundance in both LSL-Kras^{G12D}/p53$^{fl/fl}$ (KP) and LSL-Kras^{G12D}/p53$^{fl/fl}$/LKO (KPL) tumours for glucose, citrate, G6P and ADP. *P* and R^2 values were calculated using simple linear regression. **d**, Pixel-by-pixel analysis of metabolite pools from Kras^{G12D}/p53$^{fl/fl}$ (KP) and LSL-Kras^{G12D}/p53$^{fl/fl}$/LKO (KPL) tumours for glucose, citrate, G6P and ADP (mean ± standard error, *P* values indicated, two-tailed *t*-test). **e**, Schematics showing how high glycogen and glycogen metabolism support tumourigenesis. Panel **a** created with BioRender.com.

https://doi.org/10.1038/s42255-025-01243-8

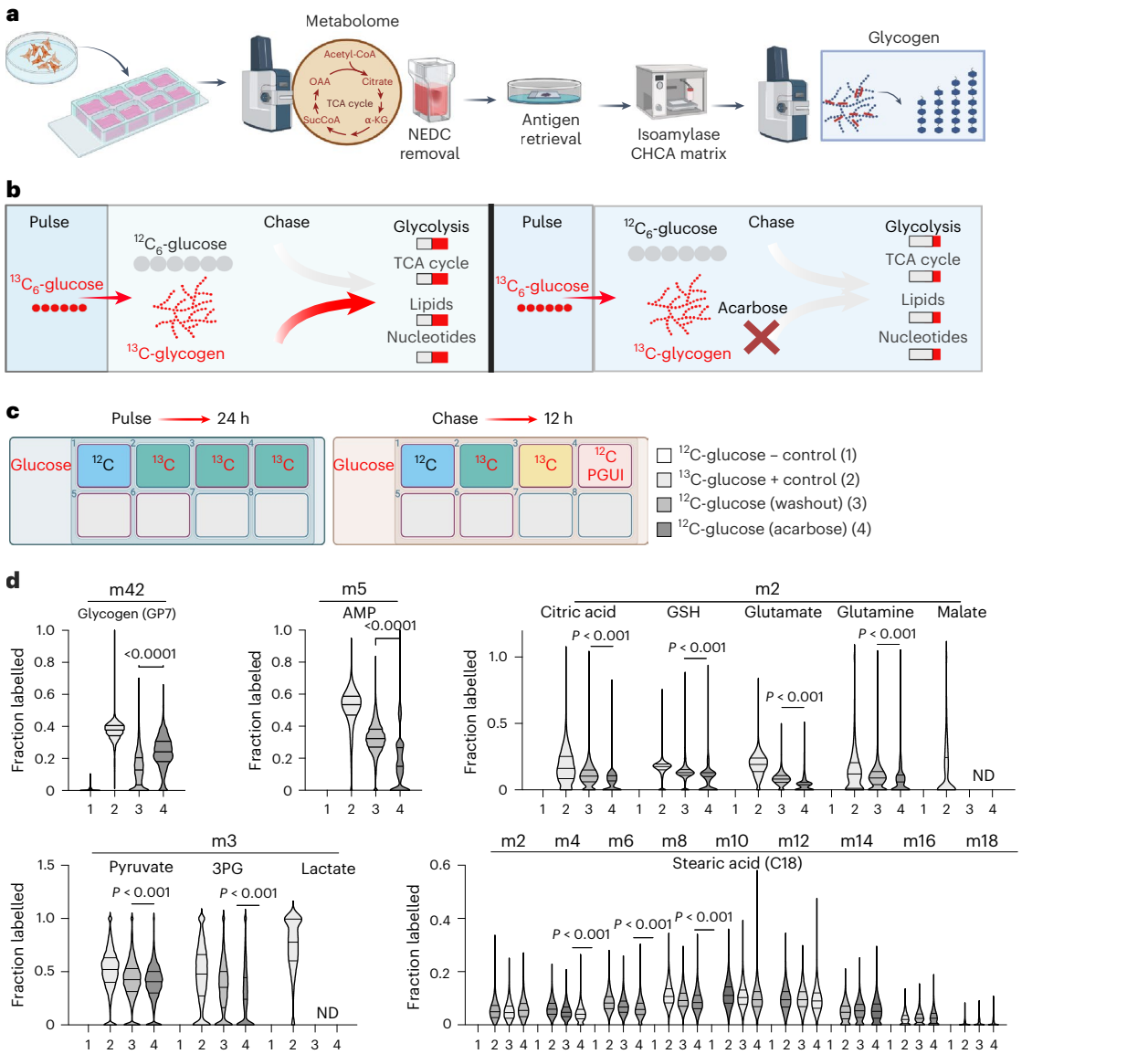

Fig. 5 | Glycogen contribution to cancer metabolism traced with ^{13}C-glucose. **a**, Schematic of the experimental workflow in a chamber well format designed to track ^{13}C labelling in the metabolome and glycogen. **b**, Schematic of using acarbose to block glycogen utilization and assess its contribution to cancer metabolism. Left: the pulse phase involves ^{13}C-glucose incorporation, followed by a chase phase to monitor its incorporation from glycogen into other metabolic pathways. Right: glycogen contribution to cancer metabolism can be blocked by the addition of acarbose, a pan inhibitor for glycogen utilization enzymes. **c**, Layout for the pulse and chase experiment using ^{13}C-glucose to pulse and ^{12}C-glucose with or without acarbose as the chase phase is depicted in a chamber well format. The four experimental conditions are (1) ^{12}C-glucose negative (−) control, (2) ^{13}C-glucose positive (+) control, (3) ^{12}C-glucose wash out after 24 h of ^{13}C-glucose enrichment and (4) ^{12}C-glucose washout after 24 h of ^{13}C-glucose enrichment with acarbose. **d**, Fraction-labelled metabolites with unique isotopologues in different metabolic pathways between vehicle and acarbose-treated groups. The group numbers correspond to what is shown in **c** (n = 6,243 unique pixels in 1, 6,387 in 2, 6,411 in 3 and 6,674 in 4; mean ± s.e.m., P values indicated, two-tailed t-test). PGUI, pan-glycogen utilization inhibitor; ND, not detected. Panels **a** and **b** created with BioRender.com.

and m3 citric acid, GSH, glutamate, glutamine and malate; m3 pyruvate, phosphoenolpyruvate, 3PG and m5 AMP; and M2/4/6/8/20-C18 fatty acid, suggesting a reduction in ^{13}C pools when glycogen utilization is blocked (Fig. 5d). Collectively, these data support that glycogen utilization directly contributes to cancer metabolism supporting multiple metabolic processes.

Discussion

Our study leveraged high-throughput spatial metabolomics screening to identify glycogen as a key oncogenic metabolite in LUAD. We demonstrated that glycogen accumulation is both pervasive in LUAD tumours and exhibits a positive association with increased tumour grade, highlighting its role in tumour progression. Furthermore, our analyses revealed a significant correlation between higher glycogen content and poorer patient survival outcomes, emphasizing the clinical relevance of this metabolic signature. Machine learning models, including AUROC and AUPRC, confirmed the robustness of glycogen as a predictive marker of LUAD mortality, with AUROC and AUPRC scores of 0.846 and 0.888, respectively. These findings suggest that glycogen could be a promising prognostic biomarker and points to the clinical utility of glycogen, where glycogen could help improve patient stratification and risk assessment.

We observed that increased glycogen levels in LUAD are associated with higher tumour grade, which led us to investigate the functional role of glycogen in driving tumour progression using well-defined mouse models. To test our hypothesis, we implemented

two complementary approaches: a dietary intervention model and a genetic model of lung cancer. In the dietary model, we exposed mice to a high-fat and high-carbohydrate diet for 2 weeks. This dietary regimen successfully elevated lung glycogen levels before the initiation of tumourigenesis in the KP LUAD mouse model. Importantly, this approach allowed us to study the direct impact of pre-tumourigenic glycogen accumulation on early tumourigenesis. In our genetic model, we engineered mice with a predisposition to accumulate glycogen in the lungs, providing a parallel system to examine the effects of sustained glycogen elevation. Both models yielded consistent results: elevated glycogen levels promoted the formation of higher-grade tumours and accelerated tumour progression in KP LUAD mice. We opted not to extend the dietary treatment beyond the initial 2 weeks for several important reasons. First, prolonged oral gavage would introduce additional stress to the mice, creating a variable that could complicate the interpretation of tumourigenesis outcomes[41]. Stress is a well-documented factor influencing cancer progression, and we aimed to minimize this potential confounder in our experimental design[41,42]. Second, it is evident that both human and KP/G mice as well as tracer analysis revealed that established tumours sustain glycogen synthesis de novo. Therefore, continuing treatment is not necessary. Importantly, a 2-week dietary exposure primed the lung tissue environment with high glycogen, creating conditions that favoured accelerated early tumourigenesis and higher-grade malignancies over the long term. This design in combination with KPL and KPG models collectively highlighted the critical role of glycogen during both early stages of tumour development as well as tumour proliferation and progression.

Our findings suggest that glycogen supports LUAD tumourigenesis through both tumour initiation and proliferation. For example, a high-fat and high-carbohydrate diet for only 2 weeks led to glycogen accumulation in the lung that gave rise to significantly increased tumour burden in the KP mice. The short dietary exposure before viral delivery suggests major roles of glycogen driving tumour initiation. This diet-induced glycogen accumulation may provide a critical substrate for the biogenetic demands of tumour initiation[12] or could influence epigenetic modifications necessary for epigenetic reprogramming[20]. However, once cancer cells are established, they maintain high glycogen levels through sustained glycogen synthesis de novo, independent of dietary input. This process is probably supported by the availability of glucose within the tumour microenvironment, ensuring a continuous supply of metabolic resources. Furthermore, it is plausible that established tumours may uptake glycogen from their microenvironment through mechanisms such as macropinocytosis[51]. However, further studies are required to elucidate the interplay between glycogen synthesis and external glycogen uptake in the tumour microenvironment, as well as to delineate the molecular pathways that drive these processes during different stages of tumour progression. Glycogen's role in tumourigenesis may extend beyond its metabolic contributions to include effects on epigenetic regulation and signalling pathways. Glycogen has been shown to influence compartmentalized regulation of acetyl-CoA, which can impact histone acetylation and, consequently, epigenetic reprogramming[20]. In addition, glycogen may promote tumourigenesis through phase separation and in negatively regulating the Hippo–YAP pathway, which is a critical tumour suppressor mechanism[21]. These multifaceted roles of glycogen could explain how dietary interventions, such as a high-fat and high-carbohydrate diet, exacerbate tumour initiation, increase tumour burden and drive more aggressive cancer phenotypes.

Phosphoproteomics and proteomics analyses of tumours from KP and KPL mice revealed that the pathogenic role of glycogen in LUAD is not through signalling. To further investigate the role of glycogen in cancer cell metabolism, we developed a multiplexed spatial metabolomics technique that enables simultaneous detection of glycogen and cellular metabolites from the same tissue sample and pixel. This approach allowed us to directly assess the spatial relationship between glycogen accumulation and metabolic reprogramming within tumours. Applying this approach, we observed strong correlations between increased glycogen levels and elevated concentrations of central carbon metabolites, such as glucose, G6P, citrate and ADP in KP tumours in vivo. These metabolites are essential for sustaining cellular proliferation and metabolic demands in tumour cells[42]. To provide direct evidence for this metabolic link, we used isotopic tracing experiments to visualize the carbon flow from glycogen to central carbon metabolic pathways. By incorporating ion mobility mass spectrometry, we accurately assessed isotopic labelling in complex molecules, such as glycogen, and precisely tracked the distribution of labelled carbon atoms across different metabolic pathways. In a high-throughput multiwell format, our method allowed us to quantify the contribution of glycogen-derived carbons to key metabolic processes, including glycolysis, the tricarboxylic acid (TCA) cycle, nucleotide biosynthesis and fatty acid synthesis. These findings underscore the role of glycogen as a metabolic driver that fuels multiple biochemical pathways. Further research should focus on which of these glycogen-supported pathways are necessary for tumour growth and progression.

This study outlines a blueprint for leveraging next-generation spatial metabolomics technologies to generate hypotheses from human tissue samples and then rigorously test these hypotheses in mechanistically relevant mouse models. This integrated approach allows the discovery and validation of key metabolic drivers, such as glycogen, while uncovering mechanistic insights that advance scientific knowledge. By applying spatial analysis to identify glycogen as an oncogenic factor in LUAD, we tested a dietary model where high-carbohydrate and high-fat intake induced a lung glycogen phenotype in mice; this diet combination is akin to a western diet consumed in the USA[52]. These findings raise the possibilities of metabolic vulnerabilities associated with diet that should be intriguing avenues for future research, such as studying the impact of dietary patterns on lung cancer survival in human populations. Nonetheless, glycogen is not the only factor contributing to tumourigenesis. Future studies should incorporate the physiological complexity of the tumour microenvironment, including immune interactions[53], hypoxic conditions[54] and extracellular matrix components[55], to provide a more comprehensive understanding of cancer biology. Addressing these variables in conjunction with glycogen metabolism will be crucial to develop effective therapeutic strategies against LUAD.

Methods

Experimental models and subject details

A549 cells were purchased from ATCC (CCL-185) and maintained in high-glucose Dulbecco's modified Eagle medium (DMEM) supplemented with 10% foetal bovine serum. Experiments were performed at passages 5–7 from the original ATCC cell line. Deidentified human patient tissues were obtained from the University of Kentucky Biospecimen Procurement and Translation Pathology Shared Resource Facility and are institutional review board exempt. Human tissues were also preserved in neutral-buffered formalin (NBF) and paraffin embedded for long-term storage. All H&E staining was performed by the University of Kentucky Biospecimen Procurement and Translation Pathology Shared Resource Facility[56]. All animal experiments were approved by the Institutional Animal Care and Use Committee at the University of Kentucky (2017-2792) and Florida (202200000686) and conducted per ethical guidelines. Mice were housed in a climate-controlled environment (14/10 h light/dark cycle, 22 °C, ≥30% humidity) with ad libitum access to water and LabDiet 2018 chow. Animals were kept in shoebox cages (18.5 cm wide × 30 cm deep × 12 cm high) with corncob bedding and nesting material. Indirect sentinels monitored colony health. Studies used ~4-month-old mice. The KP (LSL:KRASG12D/+/p53flox/flox) model was obtained from the Brainson lab, while the Epm2a$^{-/-}$ (LKO) and Gys1fl/fl models were from prior studies[57,58] and the Roach laboratory, respectively. KP mice were crossed with LKO (KPL) and

Gys1fl/fl (KPG) models to study glycogen metabolism in lung cancer. No statistical methods were used to predetermine sample sizes, but our sample sizes are similar to those reported in previous publications[59,60]. Because no sex differences had been previously reported in these mouse models, male and female mice were included and co-analysed without exclusion or segregation. Formalin-fixed paraffin-embedded (FFPE) lung tissue from KRAS (K), EGFR (E), KP, KL, KPL and KKL models were gifts from Dr Christine Brainson. All mice were randomly assigned to experimental groups, except for the KPG versus KP comparison, where group allocation was predetermined due to genetic background requirements. Mice were handled in a double-blind manner throughout euthanasia, tumour counting and MALDI imaging. Investigators conducting data analysis remained blinded to group assignments until statistical evaluation was completed.

Adeno-Cre delivery for lung tumour initiation

Adeno-Cre adenoviral vectors were acquired from University of Iowa Viral Vector Core, Iowa City, IA, USA. Vector concentration and functionality were validated via quantitative PCR and plaque assays by the manufacturer. Mice were anaesthetized using a ketamine–xylazine–saline mixture (10 µl g^{-1}). Anaesthetized mice were laid in a supine position, with their heads slightly elevated on a heating pad to maintain core body temperature. A pipette was used to administer a 62.5 µl (61.8 µl Advanced DMEM, 0.3 µl $CaCl_2$ and 0.416 µl Adeno-Cre) volume of Adeno-Cre viral solution (titre of 1×10^{10} plaque-forming units per millilitre) intranasally. Mice were monitored daily for signs of distress, changes in body weight and overall health status for endpoint euthanasia or until they were 100 days old, in accordance with Institutional Animal Care and Use Committee guidelines.

IHC

Deidentified human tissues were obtained from the University of Kentucky Biospecimen Facility. Cancer and normal tissues were fixed in NBF, paraffin-embedded and stored. Mice were euthanized by cervical dislocation, and tissues were immediately resected, fixed, embedded and stored. Sections (4 µm) were prepared for IHC[56]. Slides were dewaxed and rehydrated, and antigen retrieval was performed in Ventana CC2 buffer at 37 °C for 1 h. Primary and secondary antibody incubations were conducted at room temperature (60 min each). Antibodies included Laforin (Abcam), GYS1 (Cell Signaling) and PYGB (Proteintech). H&E staining followed standard protocols with haematoxylin, eosin, graded ethanol dehydration and coverslipping. Digital images were acquired using a ZEISS Axio Scan.Z1, and quantitative analysis was performed with Halo software (Indica Labs) using multiplex IHC and TMA modules.

Oral administration of HFCS and corn oil

D-Glucose, D-(−)-fructose and corn oil were all purchased form Sigma-Aldrich. HFCS was made at 45% glucose and 55% fructose (w/w) dissolved in autoclaved cage water before sterile filtering and administering 100 µl on the basis of a previous protocol[38]. Corn oil was sterile filtered, and 150 µl was administered. The combination diet included 100 µl HFCS and 150 µl corn oil per dose. Control mice were gavaged with 250 µl of sterile-filtered cage water. Mice were gavaged at the same time every day, Monday to Friday for 2 weeks, and their weights were recorded to ensure the supplementation was maintained within healthy parameters.

Multiplexed imaging of metabolome and glycogen from fresh frozen specimens

Mouse lungs were resected and snap frozen in liquid nitrogen. Fresh frozen lungs were cut at 10 µm onto microscope slides without optimal cutting temperature compound. Tissue sections were dried in a desiccator immediately to terminate metabolism. Slides were then sprayed with an *N*-(1-naphthyl) ethylenediamine dihydrochloride/70% methanol matrix at 7 mg ml^{-1} via an HTX M5 Sprayer. Slides were then run on Bruker timsTOF flex with a laser power operating at 10,000 Hz and 60% laser energy, with 300 laser shots per pixel, and raster and laser spot size of 50 µm to image for small molecules and lipids[61]. Mass acquisition was set from 50 to 2,000 *m/z* in negative mode. The matrix was then stripped off using ice-cold 100% methanol for 5 min, and the tissue was fixed overnight in 10% NBF. The next morning, slides were switched from NBF to 70% ethanol, and remained for 2 h before desiccating. The slides were then prepared according to our N-glycan and glycogen imaging using enzyme assist release of N-linked glycans and glycogen for MALDI ionization.

Fixed tissue sections were prepared using the HTX spray station (HTX) was used to coat the slide with a 0.2 ml aqueous solution of either isoamylase (3 units per slide), PNGase F (20 mg total per slide) or both. The spray nozzle was heated to 45 °C, and the spray velocity was 900 m min^{-1}. After enzyme application, slides were incubated at 37 °C for 2 h in a humidified chamber, then dried in a desiccator before matrix application with 0.04 g α-cyano-4-hydroxycinnamic acid matrix (CHCA) in 5.7 ml 50% acetonitrile/50% water and 5.7 µl trifluoroacetic acid) with the HTX sprayer. At the end of the sample preparation, tissue sections were run using the Bruker timsTOF flex with a laser power operating at 10,000 Hz and 60% laser energy, with 300 laser shots per pixel, and raster and laser spot size of 50 µm for the integration of metabolome and glycome using *x* ,*y* laser coordinates produced from the MALDI imaging files. Mass acquisition was set from 500 to 4,000 *m/z* in positive mode. Samples were analysed using the SCiLS labs software (Bruker) using the manufacturer-recommended settings, and pixel data were exported using the SCiLS API and plotted using graphing software Prism.

Multiplexed imaging of metabolome and glycome in chamber wells

Human lung cancer A549 cells were seeded at 60,000 cells per well on LAB-TEK 8 chamber well slides and allowed to adhere and grow overnight. For the enrichment analysis, cells were washed with 1× phosphate-buffered saline (PBS), and DMEM medium with 10% dialysed serum supplemented with 10 mM ^{13}C-glucose was added for 24, 48 and 72 h. At the end of the incubation periods, medium was aspirated, cells were washed with 0.1× PBS and cells were quenched with dehydration in a vacuum desiccator until matrix application and MALDI imaging. For the pulse-chase experiment, we used a modified protocol previously described by Xie et al.[46]; first, A549 cells were seeded in chamber wells and allowed to grow in DMEM medium supplemented with 10 mM ^{13}C-glucose to achieve glycogen enrichment at isotopic steady state. For the chase phase, A549 cells were left in either ^{13}C-glucose (positive control), 1 mM ^{12}C-glucose or 1 mM ^{12}C-glucose with 1 µM acarbose, a pan inhibitor for glycogen utilization for 12 h. At the experimental endpoint, culture medium was aspirated, and cells were washed twice with 0.1× PBS and dehydrated in a vacuum desiccator. Sequential imaging of metabolome and glycogen was similar to above, with a modified ion mobility setting to detect glycogen enrichment. Trapped ion mobility spectrometry analysis was performed using 150 V of trapped ion mobility spectrometry collision cell, $1/K_0$ (reduced ion mobility) start of 1.10 V s^{-1} cm^{-2}, $1/K_0$ end of 2.25 V s^{-1} cm^{-2}, ramp time of 200 ms, duty cycle of 16.05% and ramp rate of 4.85. CCS values were used to determine enrichment of glycogen chain length 7 having an unenriched M0 peak at an *m/z* of 1,175 and isotopologues continuing through complete enrichment of all 42 carbon atoms in the chain. ^{12}C-metabolites and their detectable ^{13}C-isotopologues were assigned using the SCILs software (for *m/z* lists, see Supplementary Tables 1–4).

Glycogen MALDI MSI in FFPE tissues

FFPE tissues were sectioned (4 µm) and mounted on slides for MALDI imaging as described[62]. Slides were heated (60 °C, 1 h), deparaffinized in xylene and rehydrated in graded ethanol and water. Antigen retrieval

was performed using citraconic anhydride buffer (pH 3) in a vegetable steamer (30 min). After cooling, buffer was gradually replaced with water, and slides were desiccated before enzymatic digestion. For absolute glycogen quantitation, serial dilutions of rabbit liver glycogen (0.05–0.00061 mg ml^{-1}) were spotted onto slides using a mosquito low-volume pipettor. Enzyme-coated slides were prepared using the HTX spray station with isoamylase (3 units per slide), PNGase F (20 mg per slide) or both, followed by incubation (37 °C, 2 h) and matrix application. MALDI MSI was performed using a Waters SynaptG2-Xs, with laser (1,000 Hz, 200 a.u., 50-µm spot), mass range (500–3,500 m/z) and ion mobility. Mass drift correction and signal enhancement were applied using high-definition imaging software[62], leveraging matrix and glycan peaks for calibration.

Fluorescence-activated cell sorting of murine lung and three-dimensional organoid culture

Mice were anaesthetized with avertin, heart was removed and lungs were inflated with 2 ml of dispase (Corning). All five lung lobes were minced and incubated in 1× PBS with 2 mg ml^{-1} collagenase/dispase (Roche) for 45 min, rotating at 37 °C. Digested tissue was filtered, pelleted and treated with red cell lysis buffer. Resulting single-cell suspensions were stained with anti-mouse-Sca1-APCCy7 (Fisher Scientific BDB560654), anti-mouse-EpCAM-PECy7 (BioLegend 118216), anti-mouse-CD31-APC (Fisher Scientific BDB551262) and anti-mouse-CD45-APC (Fisher Scientific BDB559864). Live cells were gated by exclusion of 4′,6-diamidino-2-phenylindole (DAPI, Sigma)-positive cells. All antibodies were incubated for 10–15 min at 1:100 dilutions. Cell sorting was performed with a Sony iCyt with a 100-µm nozzle. Sorted bronchioalveolar stem cells (Sca1$^+$/EpCAM$^+$/CD31$^-$/CD45$^-$/DAPI$^-$) were seeded at 2,500 cells per well with low-passage murine lung endothelial cells (as feeder cells) embedded in Matrigel (Corning, 50/50 v/v) in 0.4-µm pore transwell inserts. Organoids derived from these cultures have both bronchiolar and alveolar features[56,63]. To the bottom chamber, 500 µl of DMEM/F12 with 10% foetal bovine serum, 1× insulin–transferrin–selenium supplement and 1× GlutaMAX was added and refreshed every other day. Organoids grew over a period of 2 weeks, at which point they were quantified and isolated by dispase for further analysis.

Sample preparation for proteomics mass spectrometry

Samples for total proteome and 'mini-phos' analysis were prepared[64,65]. After lysis, protein precipitation, reduction/alkylation and digestion, peptides were quantified by micro-BCA assay and 150 µg of peptide per sample were labelled with tandem mass tag (TMT) reagents (Thermo Fisher Scientific) for 2 h at room temperature. Labelling reactions were quenched with 0.5% hydroxylamine and acidified with trifluoroacetic acid. Acidified peptides were combined and desalted by Sep-Pak (Waters). Mini-phos enrichment was performed[64] using the High Select Fe-NTA Phosphopeptide Enrichment Kit (ThermoFisher Scientific). Peptides from the flow-through were further fractionated for full proteome analysis.

Basic-pH reversed-phase separation

TMT-labelled peptides corresponding to the total proteome were solubilized in 5% acetonitrile/10 mM ammonium bicarbonate, pH 8.0, and 300 µg of TMT-labelled peptides was separated by an Agilent 300 Extend C18 column (3.5 µm particles, 4.6 mm ID and 250 mm in length). An Agilent 1260 binary pump coupled with a photodiode array detector (Thermo Scientific) was used to separate the peptides. A 45-min linear gradient from 10% to 40% acetonitrile in 10 mM ammonium bicarbonate pH 8.0 (flow rate of 0.6 ml min^{-1}) separated the peptide mixtures into a total of 96 fractions (36 s). The 96 fractions were consolidated into 24 samples in a checkerboard fashion, acidified with 20 µl of 10% formic acid and vacuum dried to completion. Twelve fractions were desalted via Stage Tips and redissolved in 5% FA/5% acetonitrile for liquid chromatography–tandem mass spectrometry level 3 (LC–MS^3) analysis.

LC–MS^3

Proteome data were acquired using an Orbitrap Eclipse mass spectrometer (ThermoFisher) with an EASY-nLC 1200. Peptides were separated on a 35-cm in-house packed column (100 µm inner diameter, Accucore, 2.6 µm, 150 Å) using a 180-min gradient at 500 nl min^{-1}. MS1 scans were collected in the Orbitrap (120,000 resolution, 50 ms maximum injection, automatic gain control (AGC) 1×10^5). MS2 scans used collision-induced dissociation fragmentation in the ion trap (0.5 Da isolation, normalized collision energy (NCE) 35%, 35 ms maximum injection, AGC 1.5×10^4) with a 90 s dynamic exclusion. MS3 scans were triggered via Orbiter and collected in the Orbitrap (50,000 resolution, NCE 45%, 200 ms maximum injection, AGC 1.5×10^5), with a close-out of two peptides per protein per fraction[66]. Phosphoproteomics used an Eclipse with an EASY-nLC 1000 and a 120-min gradient. High-field asymmetric waveform ion mobility spectrometry voltages were −40/−60/−80 V (first shot) and −45/−65 V (second shot)[67]. MS2 scans used higher-energy collisional dissociation (0.5 Da isolation, 50,000 resolution, NCE 36%, 250 ms maximum injection, AGC 1.5×10^5) with a 90 s exclusion and 1.25 s cycle time.

Proteomic data analysis

Raw files were converted to mzXML, and monoisotopic peaks were reassigned using Monocle[68]. Peptide identification was performed using the Sequest algorithm against a Uniprot mouse database (July 2014) with a 50-ppm precursor ion tolerance. Fragment ion tolerances were set to 1.0005 Da (ion trap) and 0.02 Da (Orbitrap). Static modifications included TMT (+229.1629 Da, lysine/N-termini) and carbamidomethylation (+57.0215 Da, cysteine), while oxidation (+15.9949 Da, methionine) and phosphorylation (+79.9663 Da, serine/threonine/tyrosine) were variable. Peptide-spectrum matches were filtered to 1% false discovery rate, followed by protein-level false discovery rate filtering. Phosphorylation site localization was determined using AScore[69]. Reporter ion quantification used a 0.003 Da window, selecting the most intense m/z, with correction for isotopic impurities. Peptides with a summed signal-to-noise ratio ≥100 across TMT channels were retained. Phosphorylated peptides were further filtered for isolation purity ≥0.5. Protein and phosphorylation site quantification was based on summed TMTpro signal-to-noise ratio values, with total protein normalization applied across channels to account for loading differences.

Blood glucose measurements

Blood glucose and glucose tolerance tests were performed using a glucose meter[70]. In brief, mice were monitored daily for weight and blood glucose levels. After a 6-h fast, blood glucose levels were measured by a handheld glucometer (Nova Max Plus; received from American Diabetes Wholesale), using 0.3 µl of blood from the tail vein.

Kaplan–Meier survival analysis and gene expression analysis from open-source databases

Kaplan–Meier survival analysis was performed using KM plotter[71]. In brief, RNA sequencing expression and survival data from TCGA and Genotype-Tissue Expression (GTEx) project were used to perform the Kaplan–Meier survival analysis of Laforin (Affy ID 205231_s_at) in patients with LUAD (n = 1308) and squamous cell carcinoma (n = 931). Overall survival was used as the endpoint. Samples were stratified by upper quartile. Gene expression analysis of normal and cancer samples was performed by Gene Expression Profiling Interactive Analysis (GEPIA) with matched TCGA normal and GTEx datasets. Both LUAD (tumour 483, normal 347) and LUSC (tumour 486, normal 338) were used for this analysis.

Magnetic resonance imaging and ^{1}H lung imaging

Magnetic resonance images were acquired on a 7 T Bruker BioSpec system with a 115-mm bore equipped with a maximum gradient strength of 670 mT m^{-1} and a risetime of 120 µs. Mice were anaesthetized with isoflurane inhalation and kept warm using circulating water heated to 42 °C. Images were acquired with a 59/36 mm quadrature ^{1}H volume TR coil. T1-weighted coronal images used the gradient echo fast low-angle shot (FLASH) sequence with 18 slices, repetition time 278 ms, echo time 2.4 ms, flip angle (α) = 38°, 5 averages, field of view 30 × 30 mm^2, 1 mm slice thickness and matrix size 256 × 256. All images were gated to the animal's respiratory cycle to remove breathing artefacts (SA Instruments).

Random forest predictive model of glycogen

The lung cancer cohort, which consisted of 274 patients, was profiled by TMA data focusing on nine glycogen peaks, which included '1175', '1337', '1499', '1661', '1823', '1985', '2147' and '2309'. To demonstrate that glycogen can clinically diagnose the patients, we developed a predictive model for the clinical outcome (for example, mortality status) to evaluate the predictive power of glycan. Specifically, the mortality status for the cohort, which include 128 alive and 146 dead patients based on the last censoring time, was treated as the clinical outcome. The features were normalized signals of nine glycogen peaks across all 274 patients. Without loss of generality, we adopted a random forest model as the predictive model to use glycogen signals to predict the mortality status. We adopted a leave-one-fold-out strategy to create a training and testing set by splitting the data evenly to five folds, with each fold stratified by the mortality status according to the entire cohort. One fold (20% of all patients) was used a testing set, and the remaining four folds (80% of all patients) were used as the training set. The average prediction was assessed by AUROC and AUPRC.

Quantification and statistical analysis

All animals and data points were included for statistical analysis. Data distribution was assumed to be normal, but this was not formally tested. Statistical analyses were carried out using GraphPad Prism. All numerical data are presented as mean ± s.e.m. Column analysis was performed using one-way or two-way analysis of variance (ANOVA) or Student's *t*-test. *P* values are indicated in the graphs. The statistical parameters for each experiment can be found in the figures and figure legends.

Reporting summary

Further information on research design is available in the Nature Portfolio Reporting Summary linked to this article.

Data availability

All MALDI files in imzML format generated in this study are available at https://sunlabresources.rc.ufl.edu. Proteomics datasets are available on ProteomeXchange at https://doi.org/10.25345/C5N01058W and accession number PXD060090. Source data are provided with this paper.

References

1. Imielinski, M. et al. Mapping the hallmarks of lung adenocarcinoma with massively parallel sequencing. *Cell* **150**, 1107–1120 (2012).
2. Russell, P. A. et al. Does lung adenocarcinoma subtype predict patient survival?: a clinicopathologic study based on the new International Association for the Study of Lung Cancer/American Thoracic Society/European Respiratory Society international multidisciplinary lung adenocarcinoma classification. *J. Thorac. Oncol.* **6**, 1496–1504 (2011).
3. Dragani, T. A. et al. Lung adenocarcinoma diagnosed at a younger age is associated with advanced stage, female sex, and ever-smoker status, in patients treated with lung resection. *Cancers* **15**, 2395 (2023).
4. Singh, S. S., Dahal, A., Shrestha, L. & Jois, S. D. Genotype driven therapy for non-small cell lung cancer: resistance, pan inhibitors and immunotherapy. *Curr. Med. Chem.* **27**, 5274–5316 (2020).
5. Zagryazhskaya, A., Gyuraszova, K. & Zhivotovsky, B. Cell death in cancer therapy of lung adenocarcinoma. *Int. J. Dev. Biol.* **59**, 119–129 (2015).
6. Keibler, M. A. et al. Metabolic requirements for cancer cell proliferation. *Cancer Metab.* **4**, 16 (2016).
7. Pavlova, N. N. & Thompson, C. B. The emerging hallmarks of cancer metabolism. *Cell Metab.* **23**, 27–47 (2016).
8. Kimmelman, A. C. & White, E. P. Autophagy and tumor metabolism. *Cell Metab.* **25**, 1037–1043 (2017).
9. Sullivan, M. R. et al. Quantification of microenvironmental metabolites in murine cancers reveals determinants of tumor nutrient availability. *eLife* **8**, e44235 (2019).
10. Prabakaran, S. Kras rewires metabolic networks. *Sci. Signal.* **9**, ec56 (2016).
11. Liu, J., Zhang, C., Hu, W. & Feng, Z. Tumor suppressor p53 and its mutants in cancer metabolism. *Cancer Lett.* **356**, 197–203 (2015).
12. DeBerardinis, R. J. & Chandel, N. S. Fundamentals of cancer metabolism. *Sci. Adv.* **2**, e1600200 (2016).
13. Martínez-Reyes, I. & Chandel, N. S. Cancer metabolism: looking forward. *Nat. Rev. Cancer* **21**, 669–680 (2021).
14. Nwosu, Z. C. et al. Uridine-derived ribose fuels glucose-restricted pancreatic cancer. *Nature* https://doi.org/10.1038/s41586-023-06073-w (2023).
15. Sanderson, S. M., Gao, X., Dai, Z. & Locasale, J. W. Methionine metabolism in health and cancer: a nexus of diet and precision medicine. *Nat. Rev. Cancer* **19**, 625–637 (2019).
16. Young, L. E. et al. In situ mass spectrometry imaging reveals heterogeneous glycogen stores in human normal and cancerous tissues. *EMBO Mol. Med.* **14**, e16029 (2022).
17. Hawkinson, T. R. & Sun, R. C. Matrix-assisted laser desorption/ionization mass spectrometry imaging of glycogen in situ. *Mass Spectr. Imag. Small Mol. Methods Protoc.* **2437**, 215–228 (2022).
18. Zhou, Z. et al. Clear cell adenocarcinoma of the urinary bladder is a glycogen-rich tumor with poorer prognosis. *J. Clin. Med.* **9**, 138 (2020).
19. Zhou, Z. et al. Clinical features, survival and prognostic factors of glycogen-rich clear cell carcinoma (GRCC) of the breast in the US population. *J. Clin. Med.* **8**, 246 (2019).
20. Sun, R. C. et al. Nuclear glycogenolysis modulates histone acetylation in human non-small cell lung cancers. *Cell Metab.* **30**, 903–916 (2019).
21. Liu, Q. et al. Glycogen accumulation and phase separation drives liver tumor initiation. *Cell* **184**, 5559–5576 (2021).
22. Curtis, M. et al. Fibroblasts mobilize tumor cell glycogen to promote proliferation and metastasis. *Cell Metab.* **29**, 141–155 (2019).
23. Deng, Y. et al. Spatial profiling of chromatin accessibility in mouse and human tissues. *Nature* **609**, 375–383 (2022).
24. Rappez, L. et al. SpaceM reveals metabolic states of single cells. *Nat. Methods* **18**, 799–805 (2021).
25. Cao, J. et al. Deciphering the metabolic heterogeneity of hematopoietic stem cells with single-cell resolution. *Cell Metab.* **36**, 209–221 (2024).
26. Sun, C. et al. Spatially resolved multi-omics highlights cell-specific metabolic remodeling and interactions in gastric cancer. *Nat. Commun.* **14**, 2692 (2023).
27. Buglakova, E. et al. Spatial single-cell isotope tracing reveals heterogeneity of de novo fatty acid synthesis in cancer. *Nat. Metab.* https://doi.org/10.1038/s42255-024-01118-4 (2024).
28. Schwaiger-Haber, M. et al. Using mass spectrometry imaging to map fluxes quantitatively in the tumor ecosystem. *Nat. Commun.* **14**, 2876 (2023).

29. Conroy, L. R. et al. Spatial metabolomics reveals glycogen as an actionable target for pulmonary fibrosis. *Nat. Commun.* **14**, 2759 (2023).
30. Hirase, H., Akther, S., Wang, X. & Oe, Y. Glycogen distribution in mouse hippocampus. *J. Neurosci. Res.* **97**, 923–932 (2019).
31. Nakamura-Tsuruta, S. et al. Comparative analysis of carbohydrate-binding specificities of two anti-glycogen monoclonal antibodies using ELISA and surface plasmon resonance. *Carbohydr. Res.* **350**, 49–54 (2012).
32. Donohue, K. J. et al. Gys1 antisense therapy prevents disease-driving aggregates and epileptiform discharges in a Lafora disease mouse model. *Neurotherapeutics* **20**, 1808–1819 (2023).
33. Oe, Y., Baba, O., Ashida, H., Nakamura, K. C. & Hirase, H. Glycogen distribution in the microwave-fixed mouse brain reveals heterogeneous astrocytic patterns. *Glia* **64**, 1532–1545 (2016).
34. Markussen, K. H. et al. The multifaceted roles of the brain glycogen. *J. Neurochem.* **168**, 728–743 (2023).
35. Lu, B. et al. Metabolic crosstalk: molecular links between glycogen and lipid metabolism in obesity. *Diabetes* **63**, 2935–2948 (2014).
36. Nilsson, L. H. & Hultman, E. Liver glycogen in man—the effect of total starvation or a carbohydrate-poor diet followed by carbohydrate refeeding. *Scand. J. Clin. Lab. Invest.* **32**, 325–330 (1973).
37. Charrez, B., Qiao, L. & Hebbard, L. The role of fructose in metabolism and cancer. *Horm. Mol. Biol. Clin. Invest.* **22**, 79–89 (2015).
38. Goncalves, M. D. et al. High-fructose corn syrup enhances intestinal tumor growth in mice. *Science* **363**, 1345–1349 (2019).
39. Escrich, R. et al. A high-corn-oil diet strongly stimulates mammary carcinogenesis, while a high-extra-virgin-olive-oil diet has a weak effect, through changes in metabolism, immune system function and proliferation/apoptosis pathways. *J. Nutr. Biochem.* **64**, 218–227 (2019).
40. Wu, B. et al. Dietary corn oil promotes colon cancer by inhibiting mitochondria-dependent apoptosis in azoxymethane-treated rats. *Exp. Biol. Med.* **229**, 1017–1025 (2004).
41. He, X.-Y. et al. Chronic stress increases metastasis via neutrophil-mediated changes to the microenvironment. *Cancer Cell* **42**, 474–486 (2024).
42. Ghaddar, N. et al. The integrated stress response is tumorigenic and constitutes a therapeutic liability in KRAS-driven lung cancer. *Nat. Commun.* **12**, 4651 (2021).
43. Worby, C. A., Gentry, M. S. & Dixon, J. E. Laforin, a dual specificity phosphatase that dephosphorylates complex carbohydrates. *J. Biol. Chem.* **281**, 30412–30418 (2006).
44. Zacharek, S. J. et al. Lung stem cell self-renewal relies on BMI1-dependent control of expression at imprinted loci. *Cell Stem Cell* **9**, 272–281 (2011).
45. McCorvie, T. J. et al. Molecular basis for the regulation of human glycogen synthase by phosphorylation and glucose-6-phosphate. *Nat. Struct. Mol. Biol.* **29**, 628–638 (2022).
46. Xie, H. et al. Glycogen metabolism is dispensable for tumour progression in clear cell renal cell carcinoma. *Nat. Metab.* **3**, 327–336 (2021).
47. Paglia, G. et al. Ion mobility derived collision cross sections to support metabolomics applications. *Anal. Chem.* **86**, 3985–3993 (2014).
48. Goldsmith, E., Fletterick, R. & Withers, S. The three-dimensional structure of acarbose bound to glycogen phosphorylase. *J. Biol. Chem.* **262**, 1449–1455 (1987).
49. Adisakwattana, S., Lerdsuwankij, O., Poputtachai, U., Minipun, A. & Suparpprom, C. Inhibitory activity of cinnamon bark species and their combination effect with acarbose against intestinal α-glucosidase and pancreatic α-amylase. *Plant Foods Hum. Nutr.* **66**, 143–148 (2011).
50. Martin, A. E. & Montgomery, P. A. Acarbose: an α-glucosidase inhibitor. *Am. J. Health Syst. Pharm.* **53**, 2277–2290 (1996).
51. Commisso, C. et al. Macropinocytosis of protein is an amino acid supply route in Ras-transformed cells. *Nature* **497**, 633–637 (2013).
52. Varani, J. Healthful eating, the Western style diet and chronic. *Approaches Poult. Dairy Vet. Sci.* **387**, 1377–1396 (2017).
53. Carbone, D. P., Gandara, D. R., Antonia, S., Zielinski, C. & Paz-Ares, L. G. Non–small-cell lung cancer: role of the immune system and potential for immunotherapy. *J. Thorac. Oncol.* **10**, 974–984 (2015).
54. Salem, A. et al. Targeting hypoxia to improve non–small cell lung cancer outcome. *J. Natl Cancer Inst.* **110**, 14–30 (2018).
55. White, E. S. Lung extracellular matrix and fibroblast function. *Ann. Am. Thorac. Soc.* **12**, S30–S33 (2015).
56. Zhang, H. et al. Lkb1 inactivation drives lung cancer lineage switching governed by polycomb repressive complex 2. *Nat. Commun.* **8**, 14922 (2017).
57. DePaoli-Roach, A. A. et al. Laforin and malin knockout mice have normal glucose disposal and insulin sensitivity. *Hum. Mol. Genet.* **21**, 1604–1610 (2012).
58. Ganesh, S. et al. Targeted disruption of the Epm2a gene causes formation of Lafora inclusion bodies, neurodegeneration, ataxia, myoclonus epilepsy and impaired behavioral response in mice. *Hum. Mol. Genet.* **11**, 1251–1262 (2002).
59. Xu, C. et al. Loss of Lkb1 and Pten leads to lung squamous cell carcinoma with elevated PD-L1 expression. *Cancer Cell* **25**, 590–604 (2014).
60. Fillmore, C. M. et al. EZH2 inhibition sensitizes BRG1 and EGFR mutant lung tumours to TopoII inhibitors. *Nature* **520**, 239–242 (2015).
61. Clarke, H. A. et al. Spatial metabolome lipidome and glycome from a single brain section. Preprint at *bioRxiv* https://doi.org/10.1101/2023.07.22.550155 (2023).
62. Stanback, A. E. et al. Regional N-glycan and lipid analysis from tissues using MALDI-mass spectrometry imaging. *STAR Protoc.* **2**, 100304 (2021).
63. Lee, J. H. et al. Lung stem cell differentiation in mice directed by endothelial cells via a BMP4–NFATc1–thrombospondin-1 axis. *Cell* **156**, 440–455 (2014).
64. Navarrete-Perea, J., Yu, Q., Gygi, S. P. & Paulo, J. A. Streamlined tandem mass tag (SL-TMT) protocol: an efficient strategy for quantitative (phospho) proteome profiling using tandem mass tag-synchronous precursor selection-MS3. *J. Proteome Res.* **17**, 2226–2236 (2018).
65. Li, J. et al. TMTpro-18plex: the expanded and complete set of TMTpro reagents for sample multiplexing. *J. Proteome Res.* **20**, 2964–2972 (2021).
66. Schweppe, D. K. et al. Full-featured, real-time database searching platform enables fast and accurate multiplexed quantitative proteomics. *J. Proteome Res.* **19**, 2026–2034 (2020).
67. Schweppe, D. K. et al. Characterization and optimization of multiplexed quantitative analyses using high-field asymmetric-waveform ion mobility mass spectrometry. *Anal. Chem.* **91**, 4010–4016 (2019).
68. Rad, R. et al. Improved monoisotopic mass estimation for deeper proteome coverage. *J. Proteome Res.* **20**, 591–598 (2020).
69. Beausoleil, S. A., Villén, J., Gerber, S. A., Rush, J. & Gygi, S. P. A probability-based approach for high-throughput protein phosphorylation analysis and site localization. *Nat. Biotechnol.* **24**, 1285–1292 (2006).
70. Juras, J. A. et al. In situ microwave fixation provides an instantaneous snapshot of the brain metabolome. *Cell Rep. Methods* **3**, 100455 (2023).

71. Tang, Z. et al. GEPIA: a web server for cancer and normal gene expression profiling and interactive analyses. *Nucleic Acids Res.* **45**, W98–W102 (2017).

Acknowledgements

This study was supported by National Institute of Health (NIH) grants R01AG066653, R01CA266004, R01AG078702, R01CA288696, V-Scholar Grant, and RM1NS133593 to R.C.S., R35NS116824 to M.S.G., R35GM142701 to L.C., T32HL134621 to H.A.C., and R01CA237643 and P20GM121327-03 to C.F.B. This research was also supported by the Biospecimen Procurement and Translational Pathology Shared Resource Facility of the University of Kentucky Markey Cancer Center (P30CA177558) to D.B.A. and supported in part by an NIH award, S10 OD030293, for MRI/S instrumentation. Z.L. is supported by the MBI Gator NeuroScholar Program. Large language models, for example, ChatGPT, were used to make minor grammatical improvements in the text. We thank N. R. Gough (BioSerendipity, LLC) for critical discussions and editorial assistance.

Author contributions

Conceptualization, R.C.S.; methodology, R.C.S.; investigation, H.A.C., T.R.H., C.J.S., T.M., R.A.R., L.W., J.E.C., L.E.A.Y., J.A.J., M.D.B., A.N.J., A.M., J.F.L., E.C.M., X.M., L.C., Z.L., Y.X., Y.H., X.H., A.R., M.E.M., P.K.S., J.B., G.L.A., B.M.E., C.W.V.K., C.F.B., D.B.A., M.S.G. and R.C.S.; writing—original draft, R.C.S.; writing—review and editing, R.C.S., H.A.C., C.J.S., T.R.H., C.F.B., L.E.A.Y., C.W.V.K., M.S.G. and D.B.A.; funding acquisition, M.S.G. and R.C.S.; resources, M.S.G. and R.C.S; supervision, M.S.G. and R.C.S.

Competing interests

R.C.S. has received research support and consultancy fees from Maze Therapeutics. R.C.S. is a member of the Medical Advisory Board for Little Warrior Foundation. M.S.G. has research support and research compounds from Maze Therapeutics, Valerion Therapeutics and Ionis Pharmaceuticals. M.S.G. also received consultancy fee from Maze Therapeutics, PTC Therapeutics and the Glut1-Deficiency Syndrome Foundation. D.B.A. receives book royalty from Wolters Kluwer. The other authors declare no competing interests.

Additional information

Extended data is available for this paper at https://doi.org/10.1038/s42255-025-01243-8.

Supplementary information The online version contains supplementary material available at https://doi.org/10.1038/s42255-025-01243-8.

Correspondence and requests for materials should be addressed to Matthew S. Gentry or Ramon C. Sun.

Peer review information *Nature Metabolism* thanks the anonymous reviewers for their contribution to the peer review of this work. Primary Handling Editor: Alfredo Giménez-Cassina, in collaboration with the *Nature Metabolism* team.

Reprints and permissions information is available at www.nature.com/reprints.

Publisher's note Springer Nature remains neutral with regard to jurisdictional claims in published maps and institutional affiliations.

[1]Department of Biochemistry and Molecular Biology, College of Medicine, University of Florida, Gainesville, FL, USA. [2]Center for Advanced Spatial Biomolecule Research, University of Florida, Gainesville, FL, USA. [3]Evelyn F. and William L. McKnight Brain Institute, University of Florida, Gainesville, FL, USA. [4]Department of Biostatistics College of Public Health and Health Professions and College of Medicine, University of Florida, Gainesville, FL, USA. [5]Health Outcomes & Biomedical Informatics, College of Medicine, University of Florida, Gainesville, FL, USA. [6]Regenstrief Institute, Indianapolis, IN, USA. [7]Department of Biostatistics and Health Data Science, School of Medicine, Indianapolis, IN, USA. [8]Department of Neuroscience, College of Medicine, University of Kentucky, Lexington, KY, USA. [9]Markey Cancer Center, University of Kentucky, Lexington, KY, USA. [10]Department of Molecular and Cellular Biochemistry, College of Medicine, University of Kentucky, Lexington, KY, USA. [11]Department of Toxicology and Cancer Biology, College of Medicine, University of Kentucky, Lexington, KY, USA. [12]Department of Pathology and Laboratory Medicine, College of Medicine, University of Kentucky, Lexington, KY, USA. [13]These authors contributed equally: Harrison A. Clarke, Tara R. Hawkinson. [14]These authors jointly supervised this work. ✉e-mail: matthew.gentry@ufl.edu; ramonsun@ufl.edu

https://doi.org/10.1038/s42255-025-01243-8

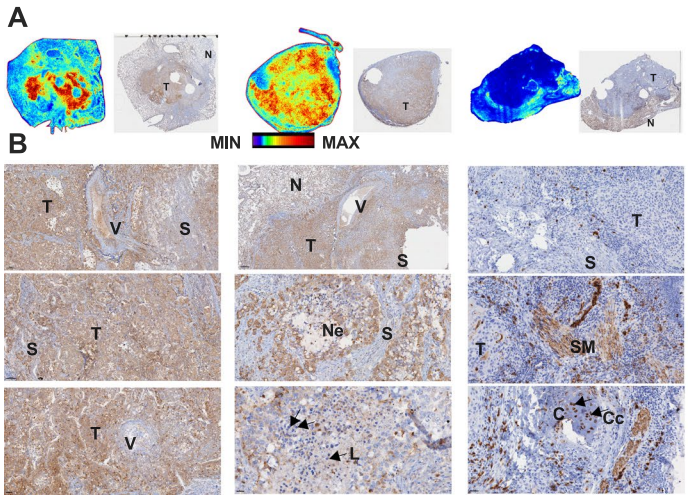

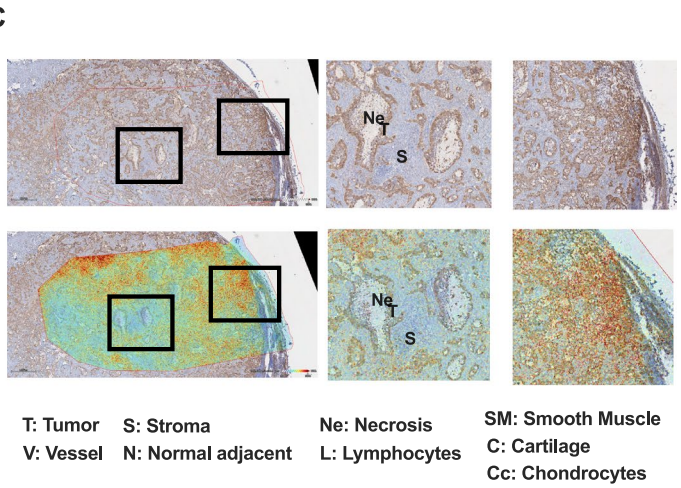

Extended Data Fig. 1 | Validation of MALDI glycogen imaging with anti-glycogen antibody staining in lung adenocarcinoma (LUAD) and lung squamous cell carcinoma (LUSC) tissues. a, Representative images of MALDI glycogen imaging (left) and corresponding anti-glycogen antibody staining (right) in two LUAD and one LUSC patient tissue samples. **b**, Detailed view of various tumor regions stained with anti-glycogen antibody showing predominately tumors positive for glycogen similar to MALDI analysis. Labels indicate tumor (T), stroma (S), normal adjacent tissue (N), vessels (V), necrosis (Ne), smooth muscle (SM), cartilage (C), and chondrocytes (Cc). **c**, Tissue overlays combining anti-glycogen antibody staining and MALDI glycogen imaging performed in SCILs software. The upper panels show the antibody staining with outlined regions for zoomed-in views, and the lower panels display the corresponding MALDI imaging overlays. c and c represent three biological replicates (individual patients). Black boxes indicate areas magnified in the zoomed-in images to illustrate the concordance between glycogen imaging and antibody staining.

https://doi.org/10.1038/s42255-025-01243-8

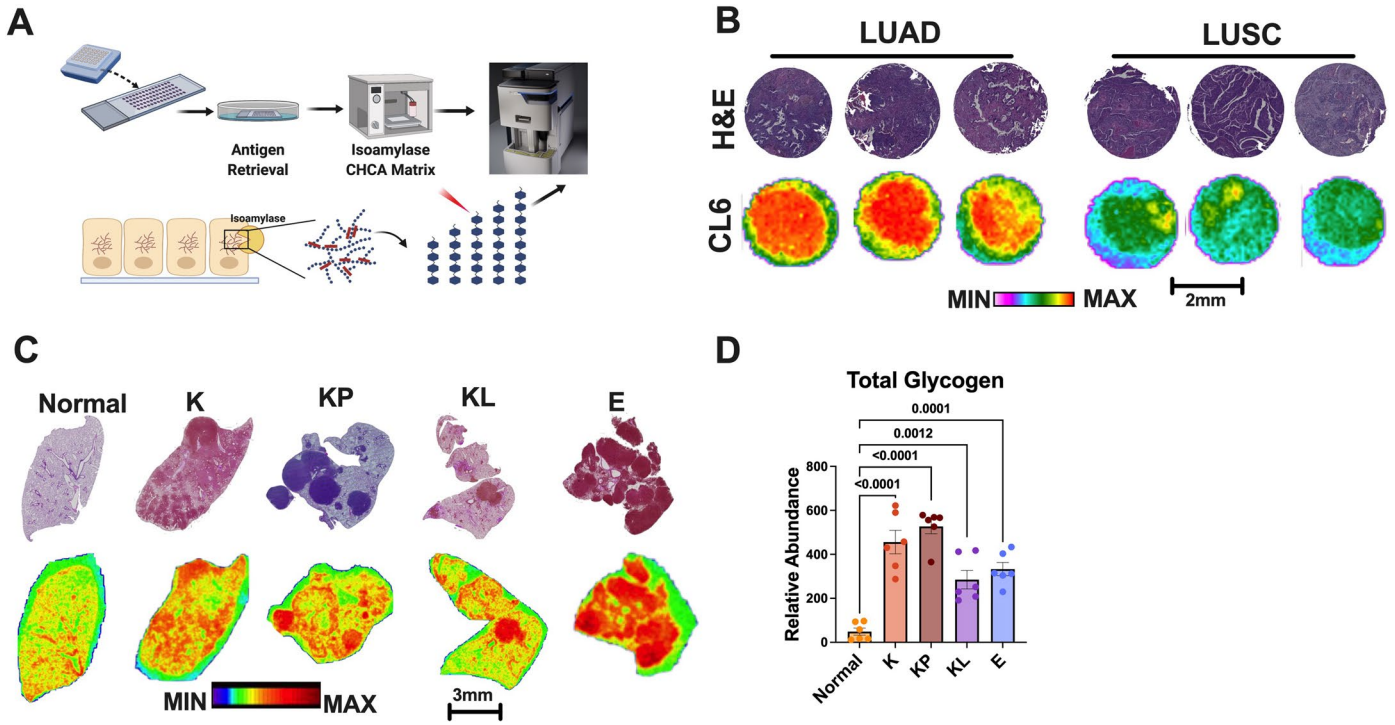

Extended Data Fig. 2 | MALDI glycogen imaging workflow and profiling of human tissue microarray (TMA) and mouse GEMM tumors. a, Schematic of the MALDI glycogen imaging workflow. Tissue sections are subjected to antigen retrieval, followed by treatment with isoamylase and application of the CHCA matrix. The isoamylase enzyme digests glycogen into glucose polymers, which are then detected and visualized using MALDI mass spectrometry. Created with BioRender.com. **b**, Representative H&E staining (top row) and MALDI glycogen imaging (bottom row) of lung adenocarcinoma (LUAD) and lung squamous cell carcinoma (LUSC) tissue cores from a TMA, image represents single run from three repeats, Scale bar: 2 mm. **c**, Representative H&E staining (top row) and MALDI glycogen imaging (bottom row) of normal lung tissue and various genetically engineered mouse model (GEMM) tumors. The GEMM tumors include K (Kras), KP (Kras; Pten), KL (Kras; Lkb1), and E (Egfr). Scale bar represents 3 mm. **d**, Quantification of total glycogen levels in normal lung tissue and GEMM tumors, as measured by MALDI glycogen imaging. Bar graph shows the relative abundance of glycogen in normal, K, KP, KL, and E tissues (n = 6/group; mean +/−s.e.m. *p*-values indicated; one-way ANOVA and Tukey's multiple comparison test).

https://doi.org/10.1038/s42255-025-01243-8

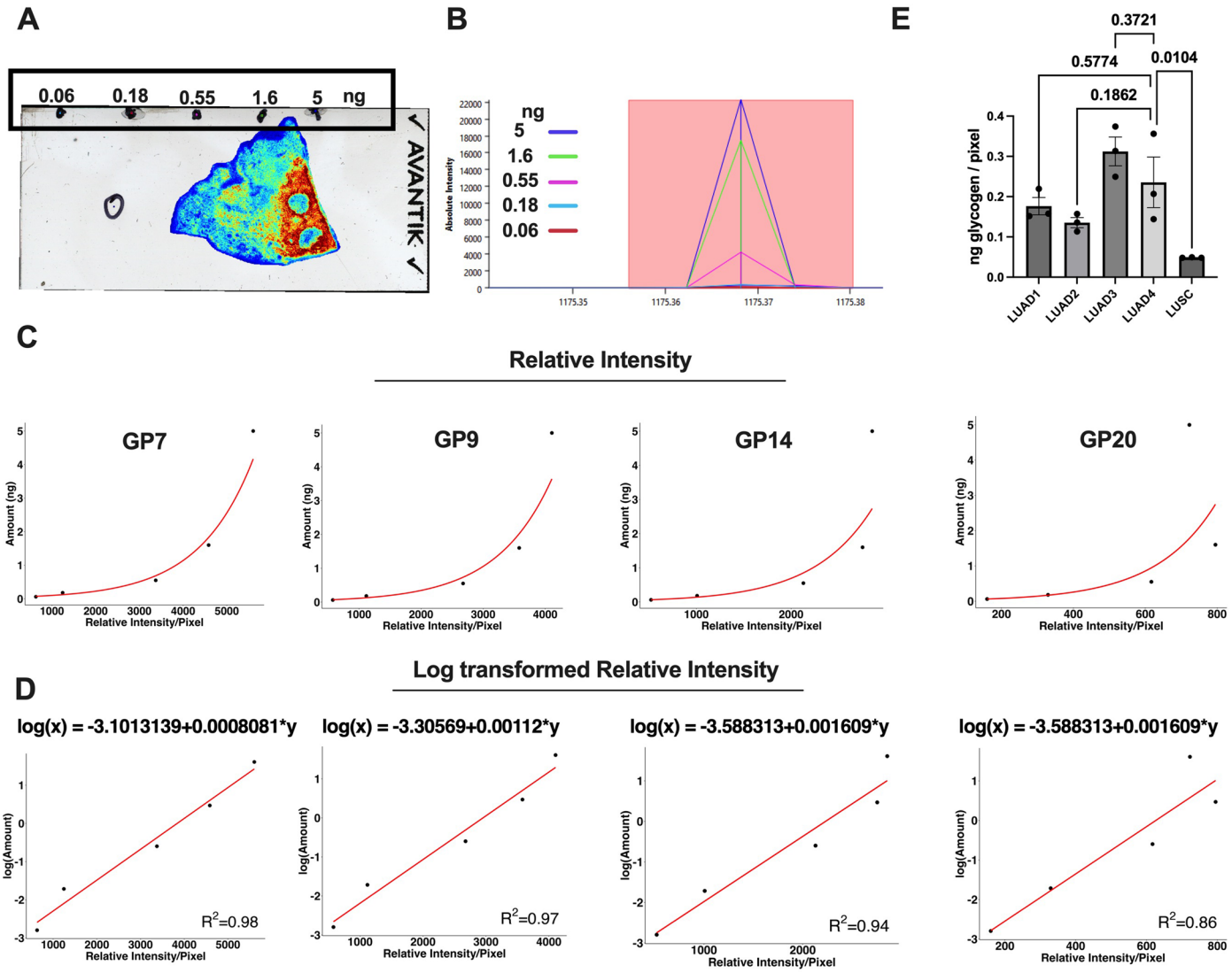

Extended Data Fig. 3 | Determination of absolute glycogen concentration using spotted standards by MALDI imaging. a, Scanned image showing the location of spotted glycogen standards (0.06, 0.18, 0.55, 1.6, and 5 ng) next to a tissue section on a microscope slide. **b**, Mass spectra of different glycogen concentrations spotted on the slide, indicating the glucose polymer 7 m/z peaks corresponding to varying amounts of glycogen. **c**, XY plots showing the relationship between glycogen concentration (ng) and relative intensity per pixel for each spotted standard. **d**, Log-transformed plots of relative intensity versus glycogen concentration for the standards for different glucose chain length indicated above. The linear regression lines indicate the strong correlation used for glycogen quantification. R^2 values for each plot are shown, line equations are displayed on top. **e**, Absolute quantification of glycogen in four human lung adenocarcinoma (LUAD) and one lung squamous cell carcinoma (LUSC) tissue sections (n = 3 ROIs of 500 pixels/tissue; mean +/− s.e.m. *p*-values indicated; one-way ANOVA adjusted for Tukey's multiple comparisons).

https://doi.org/10.1038/s42255-025-01243-8

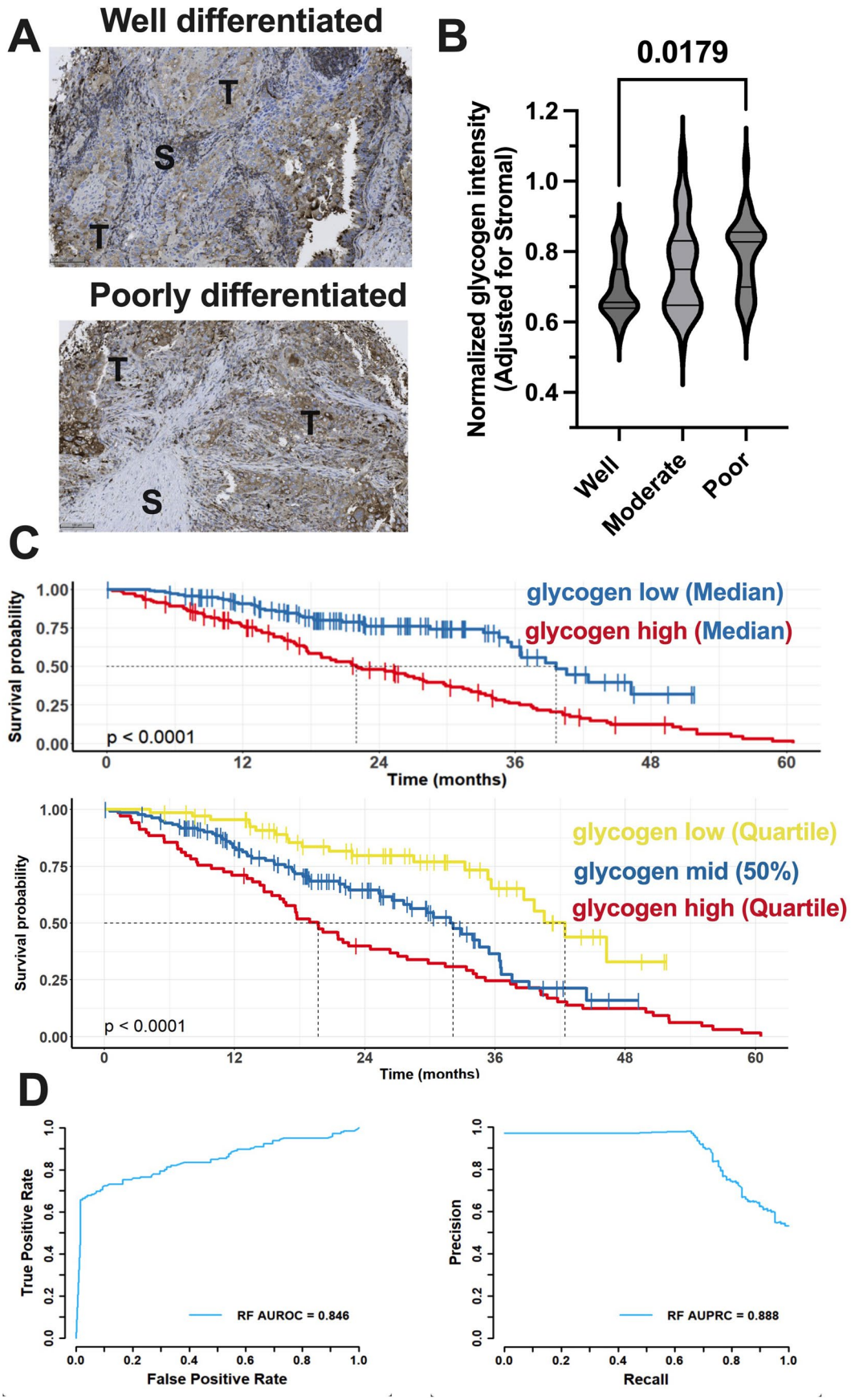

Extended Data Fig. 4 | See next page for caption.

https://doi.org/10.1038/s42255-025-01243-8

Extended Data Fig. 4 | Glycogen accumulation correlates with tumor grade and predicts survival outcomes. a, Representative immunohistochemical staining of glycogen in well differentiated (top) and poorly differentiated (bottom) tumour regions. T, tumour tissue; S, stromal tissue. **b**, Quantification of normalized glycogen intensity (adjusted for stromal regions) across tumour samples stratified by differentiation status: well, moderate, and poor in 247 LUAD patients (mean +/- s.e.m. *p*-values indicated). **c**, Kaplan-Meier survival curves illustrating the relationship between glycogen levels and patient survival. Top: Patients divided by the median glycogen expression level (low vs. high). Bottom: Survival analysis stratified into glycogen low (quartile), mid (50th percentile), and high (quartile) groups. Log-rank test *p*-value indicates a significant association between high glycogen content and decreased survival ($p < 0.0001$). **d**, Predictive performance of a random forest model for glycogen intensity in relation to survival outcomes, shown through the area under the receiver operating characteristic (AUROC = 0.846) and the area under the precision-recall curve (AUPRC = 0.888).

https://doi.org/10.1038/s42255-025-01243-8

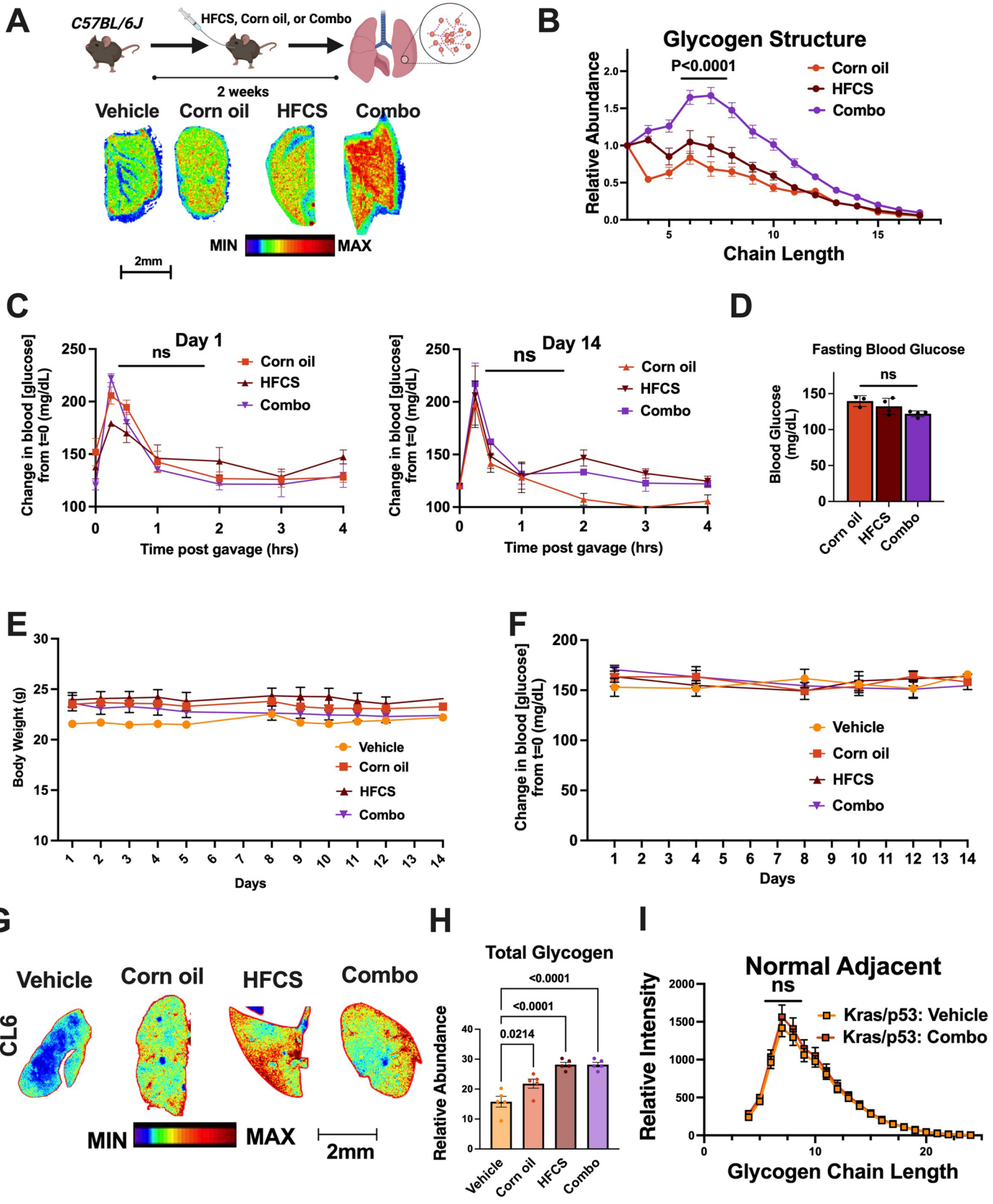

Extended Data Fig. 5 | See next page for caption.

https://doi.org/10.1038/s42255-025-01243-8

Extended Data Fig. 5 | Impact of different diets on glycogen and glucose metabolism in C57BL/6 J mice. a, Top: Schematic of the experimental design where C57BL/6 J mice were fed with vehicle, corn oil, high-fructose corn syrup (HFCS), or a combination (Combo) diet for 2 weeks. Created with BioRender.com. Bottom: MALDI glycogen imaging of lung tissues from mice subjected to different dietary treatments. Scale bar: 2 mm. **b**, Glycogen structure analysis in the lung tissues of WT mice treated with different diets. The graph shows the relative abundance of glycogen chain lengths in mice fed with corn oil, HFCS, or the Combo diet (n = 3 mice; mean +/− s.e.m. *p*-values indicated; two-way ANOVA adjusted for Tukey's multiple comparisons). **c**, Glucose tolerance test results for mice on Day 1 (left) and Day 14 (right) post-treatment. The graphs show changes in blood glucose levels (mg/dL) over time following glucose gavage. No significant differences (ns) were observed among the different diet groups (n = 3 mice; mean +/− s.e.m. *p*-values indicated; two-way ANOVA adjusted for Tukey's multiple comparisons). **d**, Fasting blood glucose levels (mg/dL) in the same cohort of mice. No significant differences (ns) were observed among the different diet groups (n = 3 mice; mean +/− s.e.m. *p*-values indicated; two-way ANOVA adjusted for Tukey's multiple comparisons). **e**, Body weight (g) of mice over the 14-day treatment period, showing no significant differences among the diet groups (n = 3 mice; mean +/− s.e.m. *p*-values indicated; two-way ANOVA adjusted for Tukey's multiple comparisons). **f**, Changes in blood glucose levels (mg/dL) over the 14-day treatment period, showing no differences among the diet groups (n = 3 mice; mean +/− s.e.m. *p*-values indicated; two-way ANOVA adjusted for Tukey's multiple comparisons). **g**, Liver glycogen imaging using CL6 staining in mice fed with vehicle, corn oil, HFCS, or the Combo diet. Scale bar: 2 mm. **h**, Quantification of total glycogen in liver tissues from mice subjected to different dietary treatments (n = 3 mice; mean +/− s.e.m. *p*-values indicated; one-way ANOVA adjusted for Tukey's multiple comparison). **i**, Glycogen chain length analysis in normal adjacent tissues from KP and KP Combo-treated mice related to Fig. 3. The graph shows the relative intensity of glycogen chain lengths, (n = 6 mice; mean +/− s.e.m. two-way ANOVA for Tukey's multiple comparison).

https://doi.org/10.1038/s42255-025-01243-8

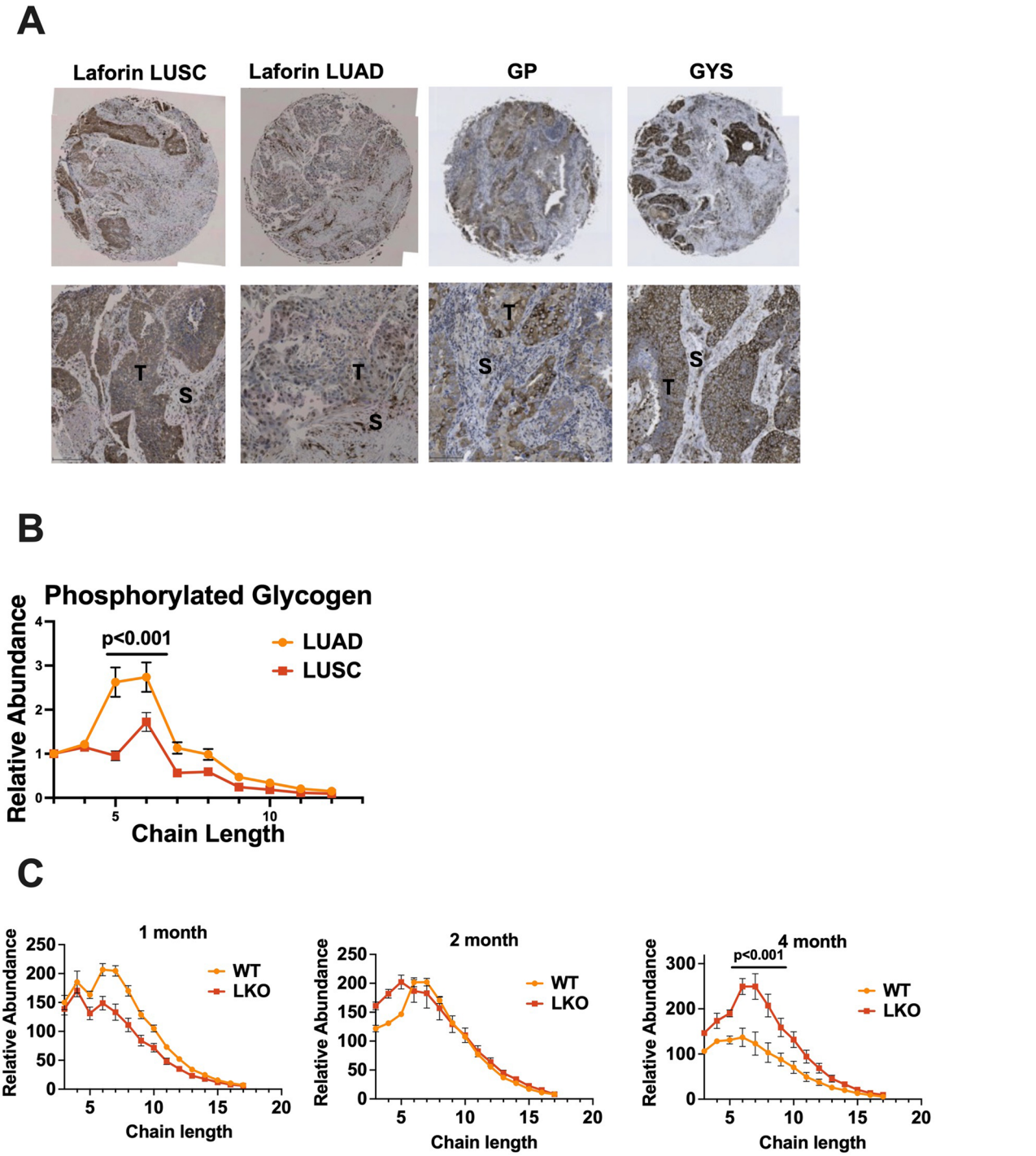

Extended Data Fig. 6 | Laforin expression, phosphorylated glycogen analysis, and glycogen dynamics in LKO animals. a, Representative IHC images of tissue cores and zoomed-in views stained with antibodies against Laforin in LUSC (leftmost), Laforin in LUAD (second from left), GP (glycogen phosphorylase), and GYS (glycogen synthase,), image represents single replicates from three repeats. **b**, Phosphorylated glycogen chain length analysis in LUAD and LUSC tissue cores from TMA (n = 67 patients for LUAD, 52 for LUSC, mean +/− s.e.m. *p*-values indicated; two-way ANOVA adjusted for Tukey's multiple comparisons). **c**, Glycogen chain length analysis in the lungs of WT and LKO (Laforin knockout) mice over 1-, 2, and 4- months (n = 4 animals/group mean +/−s.e.m. *p*-values indicated; two-way ANOVA adjusted for Tukey's multiple comparisons).

https://doi.org/10.1038/s42255-025-01243-8

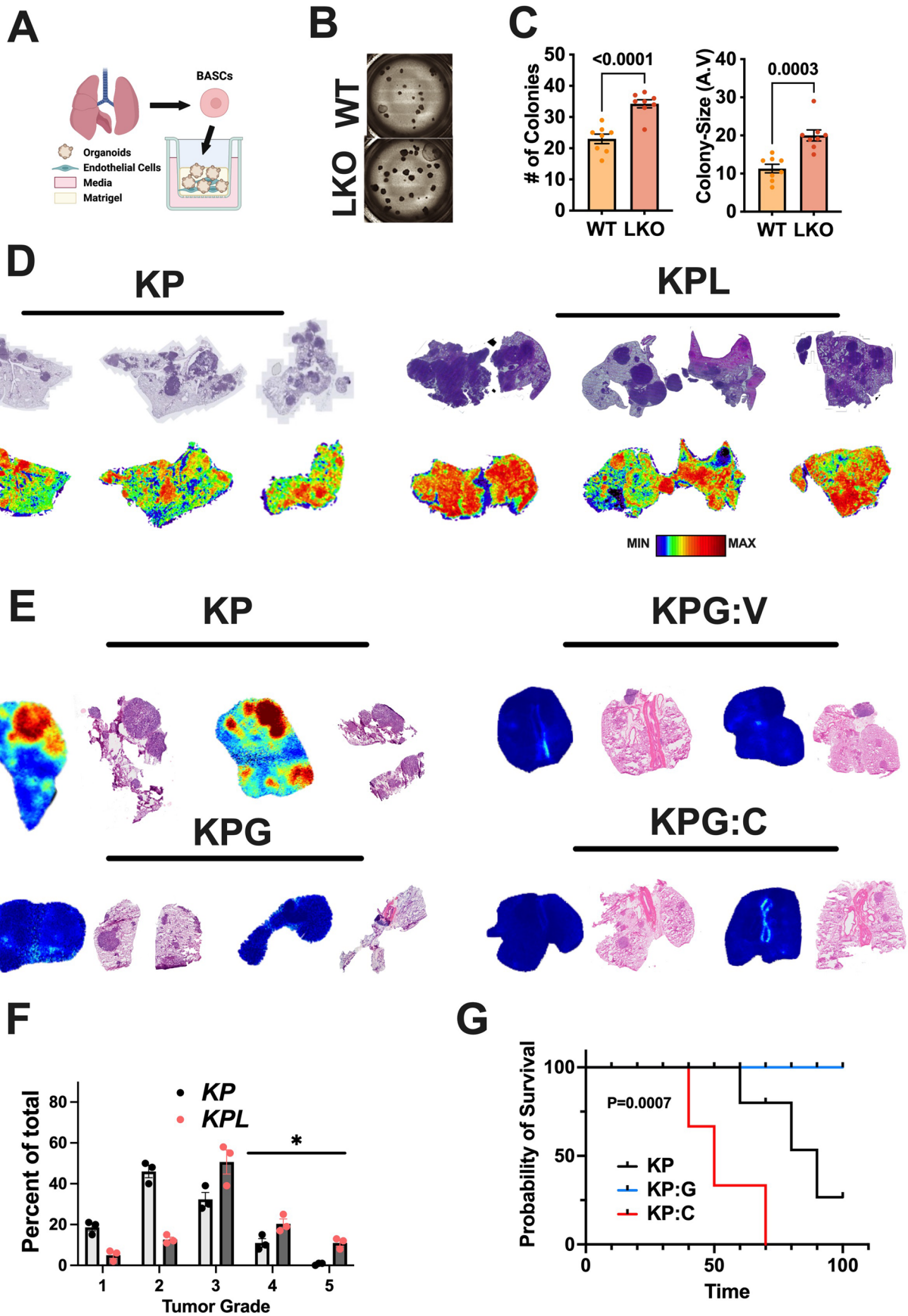

Extended Data Fig. 7 | See next page for caption.

https://doi.org/10.1038/s42255-025-01243-8

Extended Data Fig. 7 | Lung stem cell growth in vitro, H&E and MALDI glycogen imaging of different mouse models. a, Schematic of isolating bronchoalveolar stem cells and differentiation to bronchiolar and alveolar organoids in matrigel. **b**, Representative bright field images of bronchiolar and alveolar organoids derived from WT and laforin$^{-/-}$ (LKO) animals. **c**, Number of colonies and colony size from bronchiolar and alveolar organoids derived from WT and laforin$^{-/-}$ (LKO) animals. Values are presented as mean +/− s.e.m. *p*-values were calculated using two-tailed *t*-test. **d**, Additional representative H&E images and MALDI imaging of an adjacent tissue section showing tumor formation and glycogen levels LSL-Kras^{G12D}/p53$^{fl/fl}$ (KP) and LSL-Kras^{G12D}/p53$^{fl/fl}$ /LKO(KPL) (n = 3 each). **e**, Additional representative H&E images and MALDI imaging of an adjacent tissue section showing tumor formation and glycogen levels LSL-Kras^{G12D}/p53$^{fl/fl}$ (KP); LSL-Kras^{G12D}/p53$^{fl/fl}$/Gys$^{fl/fl}$ (KPG); LSL-Kras^{G12D}/p53$^{fl/fl}$/Gys$^{fl/fl}$:Vehicle (KPG:V); LSL-Kras^{G12D}/p53$^{fl/fl}$/Gys$^{fl/fl}$:Combination diet (KPG/C)animals (n = 2 each). **f**, Distribution of tumor grades across KP and KPL cohorts of mice (n = 3 mice; mean +/− s.e.m. *p*-values indicated; one-way ANOVA adjusted for Tukey's multiple comparisons). **g**. Kaplan Meier survival analysis for mice in different groups. Log-rank test stated.

https://doi.org/10.1038/s42255-025-01243-8

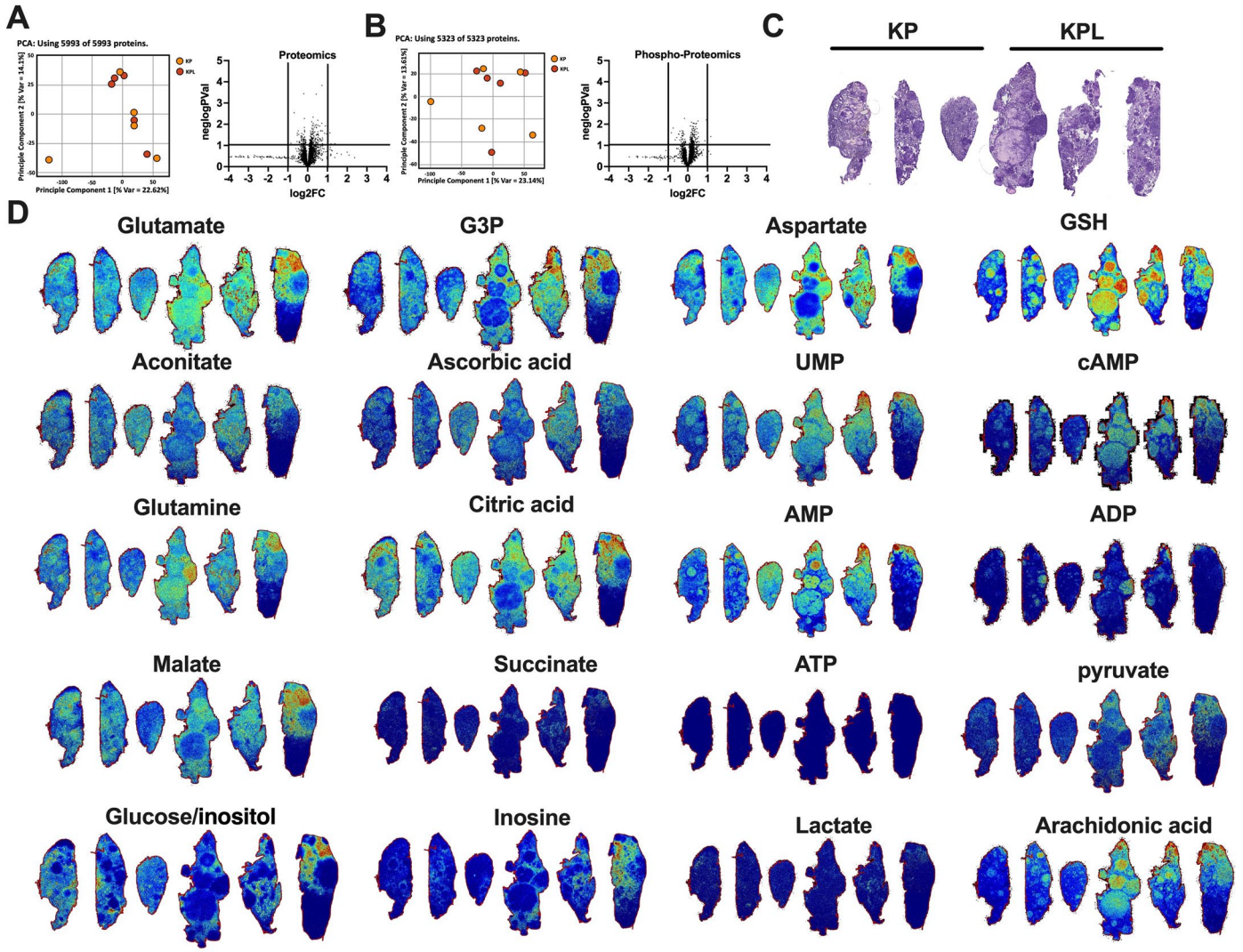

Extended Data Fig. 8 | Comparative proteomics, phosphoproteomic, and spatial metabolomics analysis in KP and KPL tumors. a, left: Principal component analysis (PCA) of 5993 proteins from proteomics data, showing no major changes between KP and KPL tumors. right: Volcano plot of proteomics data, with log2 fold change (log2FC) on the x-axis and -log10 p-value on the y-axis, indicating no significant differential expression between KP and KPL tumors. **b**, Left: Principal component analysis (PCA) of 5323 proteins from phosphoproteomic data, showing no major changes between KP and KPL tumors. Right: Volcano plot of phosphoproteomic data, with log2 fold change (log2FC) on the x-axis and -log10 p-value on the y-axis, indicating no significant differential phosphorylation between KP and KPL tumors. **c**, H&E-stained images of adjacent tissue slices used on MALDI analysis from KP (left) and KPL (right) tumors, image represents single analysis from three repeats. **d**, MALDI imaging of various metabolites in the lungs of KP and KPL GEMM tumors. Metabolites analyzed include glutamate, glycerol-3-phosphate (G3P), aspartate, glutathione (GSH), aconitate, ascorbic acid, uridine monophosphate (UMP), cyclic adenosine monophosphate (cAMP), glutamine, citric acid, adenosine monophosphate (AMP), ADP, malate, succinate, adenosine triphosphate (ATP), pyruvate, glucose/inositol, inosine, lactate, and arachidonic acid.

https://doi.org/10.1038/s42255-025-01243-8

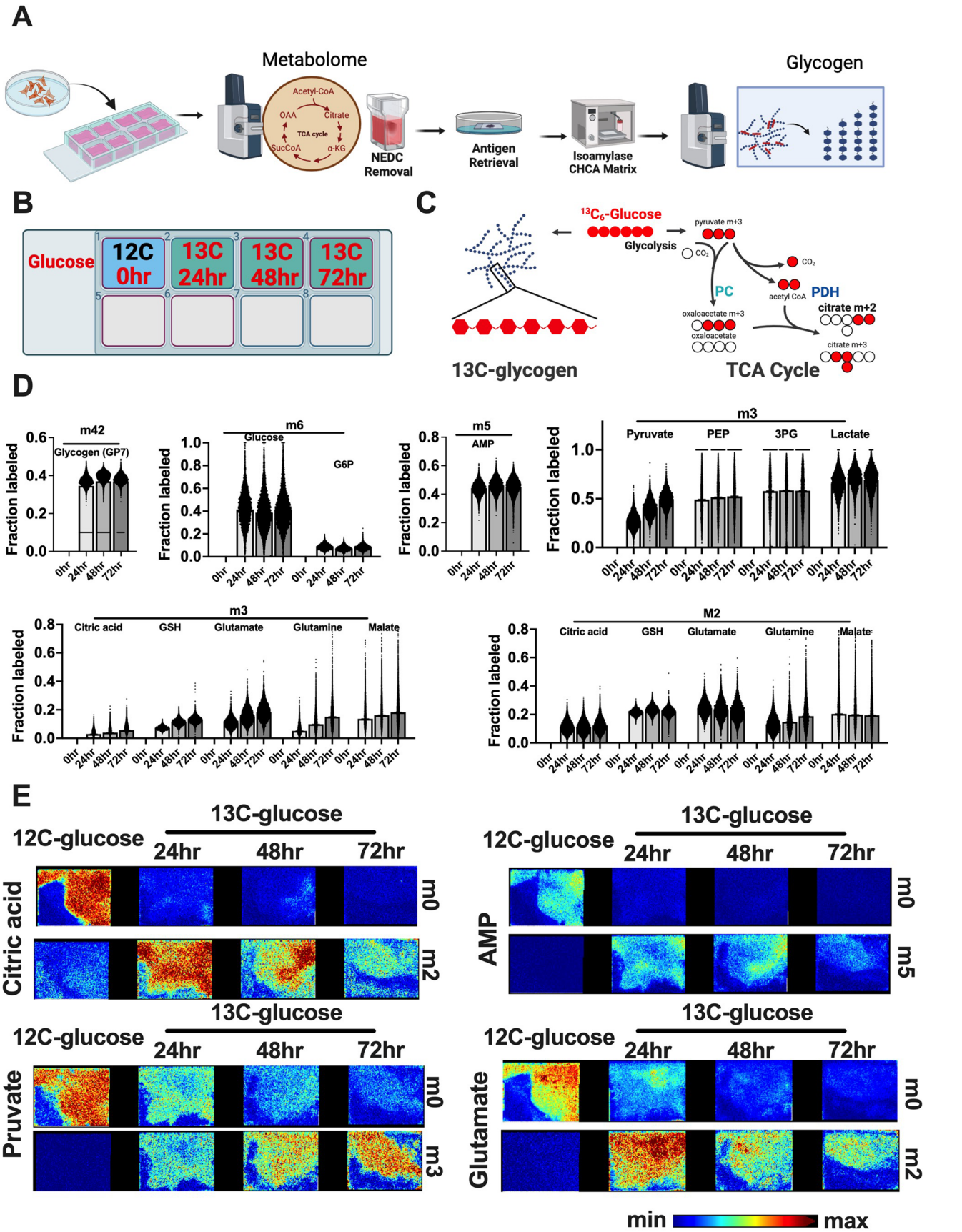

Extended Data Fig. 9 | See next page for caption.

https://doi.org/10.1038/s42255-025-01243-8

Extended Data Fig. 9 | Multiplexed spatial metabolomics and glycogen analysis with ^{13}C-glucose tracer enrichment. a, Schematic of the multiplexed spatial metabolomics and glycogen workflow. Cells grown in chamber are grown in ^{12}C- or ^{13}C-glucose. After enrichment period, cells in chamber wells are imaged for metabolomics with NEDC, followed by antigen retrieval, isoamylase treatment, and CHCA matrix application for glycogen imaging. Created with BioRender.com. **b**, Layout of tracer enrichment in a chamber well format. Cells are exposed to 12C-glucose or 13C-glucose for 24, 48, and 72 hours in different wells. **c**, Metabolic pathway of ^{13}C-glucose showing its incorporation into glycolysis and the TCA cycle, and ^{13}C-glycogen formation. Key metabolic intermediates such as pyruvate (P), phosphoenolpyruvate (PEP), citrate (Cit), and oxaloacetate (OAA) are highlighted, along with enzymes pyruvate carboxylase (PC) and pyruvate dehydrogenase (PDH). **d**, Enrichment of various isotopologues in metabolites of glycolysis, TCA cycle, nucleotides, and glycogen. Fraction labeled graphs for m42 (glycogen), m6 (glucose and G6P), m5 (AMP), m3 (pyruvate, PEP, 3PG, lactate), and m2 (citric acid, GSH, glutamate, glutamine, malate) are shown at 0, 24, 48, and 72 hours. (n = 6697 individual pixels measured by MALDI imaging. **e**, Representative examples of ^{13}C isotopologues detected through MALDI imaging, with ^{12}C-glucose wells as controls. Metabolites visualized include citric acid, AMP, pyruvate, and glutamate.

https://doi.org/10.1038/s42255-025-01243-8

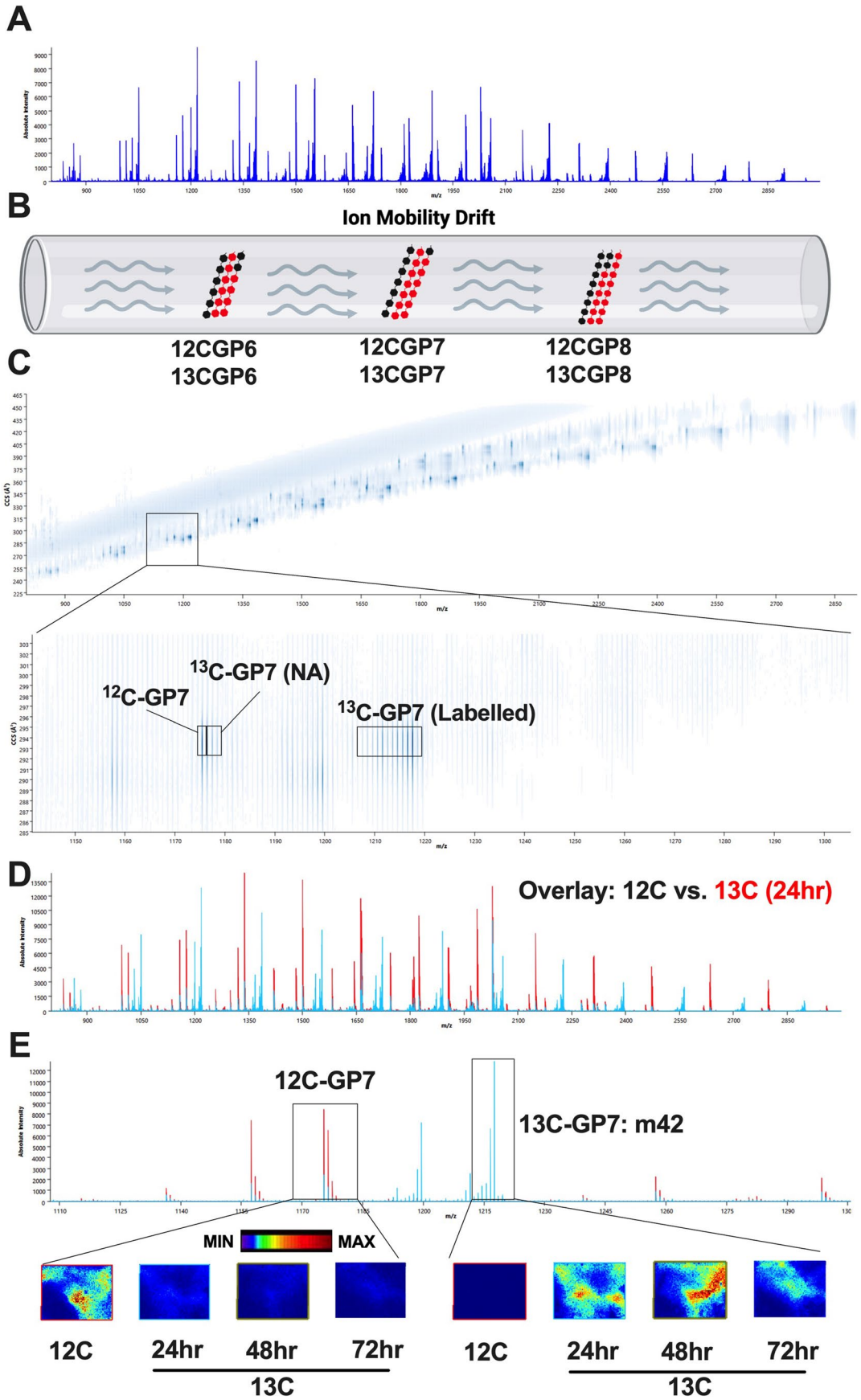

Extended Data Fig. 10 | See next page for caption.

https://doi.org/10.1038/s42255-025-01243-8

Extended Data Fig. 10 | Ion mobility and MALDI imaging of ^{12}C and ^{13}C-labeled glycogen species. a, Mass spectra showing both ^{12}C and 13C-labeled glycogen-released glucose chain lengths. **b**, Schematic of ion mobility drift separation for 13C-labeled species. The diagram illustrates how ^{12}C and ^{13}C glycogen species are separated based on their drift times in the ion mobility spectrometer. Created with BioRender.com. **c**, 2D plot of ion mobility drift time versus m/z (mass-to-charge ratio), with a zoomed-in view highlighting the separation between ^{12}C-GP7 and ^{13}C-GP7 species. The plot shows similar drift times for both ^{12}C and ^{13}C glycogen species, indicating effective alignment. **d**, Overlay of mass spectra from unlabeled (^{12}C) and ^{13}C-glucose labeled wells (24 hours) for glycogen. The overlay highlights the differences in peak intensities, indicating the incorporation of ^{13}C into the glycogen molecules. **e**, Detailed overlay of ^{12}C and ^{13}C-labeled glycogen species, showing the enrichment of fully labeled ^{13}C-GP7 at m/z 42. Representative MALDI images are included to show the spatial distribution of glycogen species at 0 (12 C), 24, 48, and 72 hours of ^{13}C labeling.

nature portfolio

Corresponding author(s): Ramon Sun

Last updated by author(s): 1/31/2025

Reporting Summary

Nature Portfolio wishes to improve the reproducibility of the work that we publish. This form provides structure for consistency and transparency in reporting. For further information on Nature Portfolio policies, see our Editorial Policies and the Editorial Policy Checklist.

Statistics

For all statistical analyses, confirm that the following items are present in the figure legend, table legend, main text, or Methods section.

n/a	Confirmed	
☐	☒	The exact sample size (*n*) for each experimental group/condition, given as a discrete number and unit of measurement
☐	☒	A statement on whether measurements were taken from distinct samples or whether the same sample was measured repeatedly
☐	☒	The statistical test(s) used AND whether they are one- or two-sided *Only common tests should be described solely by name; describe more complex techniques in the Methods section.*
☒	☐	A description of all covariates tested
☒	☐	A description of any assumptions or corrections, such as tests of normality and adjustment for multiple comparisons
☐	☒	A full description of the statistical parameters including central tendency (e.g. means) or other basic estimates (e.g. regression coefficient) AND variation (e.g. standard deviation) or associated estimates of uncertainty (e.g. confidence intervals)
☐	☒	For null hypothesis testing, the test statistic (e.g. *F*, *t*, *r*) with confidence intervals, effect sizes, degrees of freedom and *P* value noted *Give P values as exact values whenever suitable.*
☒	☐	For Bayesian analysis, information on the choice of priors and Markov chain Monte Carlo settings
☒	☐	For hierarchical and complex designs, identification of the appropriate level for tests and full reporting of outcomes
☒	☐	Estimates of effect sizes (e.g. Cohen's *d*, Pearson's *r*), indicating how they were calculated

Our web collection on statistics for biologists contains articles on many of the points above.

Software and code

Policy information about availability of computer code

Data collection	Bruker timeControl/Fleximaging V1.5, waters HDI V2.0, Akoya nstrument software HT 2.0
Data analysis	GraphPad Prism V10, Qupath V0.5.1, Akoya Phenochart 2.0,

For manuscripts utilizing custom algorithms or software that are central to the research but not yet described in published literature, software must be made available to editors and reviewers. We strongly encourage code deposition in a community repository (e.g. GitHub). See the Nature Portfolio guidelines for submitting code & software for further information.

Data

Policy information about availability of data

All manuscripts must include a data availability statement. This statement should provide the following information, where applicable:

- Accession codes, unique identifiers, or web links for publicly available datasets
- A description of any restrictions on data availability
- For clinical datasets or third party data, please ensure that the statement adheres to our policy

All MALDI files in imzML format generated in this study are available at https://sunlabresources.rc.ufl.edu. Proteomics datasets have been deposited in ProteomeXchange with the DOI: 10.25345/C5N01058W and Accession number PXD060090.

Research involving human participants, their data, or biological material

Policy information about studies with human participants or human data. See also policy information about sex, gender (identity/presentation), and sexual orientation and race, ethnicity and racism.

Reporting on sex and gender	N/A
Reporting on race, ethnicity, or other socially relevant groupings	N/A
Population characteristics	N/A
Recruitment	N/A
Ethics oversight	N/A

Note that full information on the approval of the study protocol must also be provided in the manuscript.

Field-specific reporting

Please select the one below that is the best fit for your research. If you are not sure, read the appropriate sections before making your selection.

☒ Life sciences ☐ Behavioural & social sciences ☐ Ecological, evolutionary & environmental sciences

For a reference copy of the document with all sections, see nature.com/documents/nr-reporting-summary-flat.pdf

Life sciences study design

All studies must disclose on these points even when the disclosure is negative.

Sample size	Sample size of human clinical data was based upon availability. Sample size of mouse experiments was determined based on previous animal experiments performed in the laboratory and previously published reports of KP mosue models(PMID: 24794706 and PMID: 25629630) . The sample sizes for each study are available in the methods or figure captions.
Data exclusions	No data was excluded.
Replication	All data were derived from independently replicated experiments using distinct biological samples. These experiments were independently repeated a minimum of two times, yielding consistent results across multiple repetitions. The data were generated through independent experiments using distinct biological samples. Each experiment was conducted independently and repeated a minimum of two times, producing consistent results.
Randomization	Randomization was applied at multiple levels to ensure unbiased experimental design. In vitro experiments were conducted under identical initial conditions, with cells plated into culture dishes before treatment. Cells in different dishes or wells were randomly assigned to treatment groups. Mice were randomly allocated into experimental groups for Western diet feeding and tumor growth studies, with the exception of comparisons between KP and KPG cohorts, where group allocation was predetermined by genotype. Human tissue samples were randomly spotted on tissue microarrays (TMA); however, subgroup selection was based on mutation status to facilitate targeted analyses.
Blinding	Blinding was incorporated at multiple stages of the experimental process to minimize bias and ensure objectivity. Operators were blinded to animal group assignments during euthanasia, sample collection, and subsequent analyses. MALDI imaging and data acquisition were performed without prior knowledge of sample identity. Tumor number assessment and other quantitative evaluations were conducted under blinded conditions, with investigators remaining unaware of group allocations until the final data analysis stage. This approach ensured that all experimental procedures, from sample handling to data interpretation, were conducted without bias.

Reporting for specific materials, systems and methods

We require information from authors about some types of materials, experimental systems and methods used in many studies. Here, indicate whether each material, system or method listed is relevant to your study. If you are not sure if a list item applies to your research, read the appropriate section before selecting a response.

Materials & experimental systems

n/a	Involved in the study
☐	☒ Antibodies
☐	☒ Eukaryotic cell lines
☒	☐ Palaeontology and archaeology
☐	☒ Animals and other organisms
☐	☒ Clinical data
☒	☐ Dual use research of concern
☒	☐ Plants

Methods

n/a	Involved in the study
☒	☐ ChIP-seq
☒	☐ Flow cytometry
☒	☐ MRI-based neuroimaging

Antibodies

Antibodies used

Laforin (Abcam,ab129321)
GYSl (Cell Signaling, #10371)
PYGB (Proteintech, 55380-1-AP)
anti-mouse-Sca1-APCCy7 (Fisher Scientific BDB560654)
anti-mouse-EpCAM-PECy7 (BioLegend 118216)
anti-mouse-CD31-APC (Fisher Scientific BDB551262)
anti-mouse-CD45-APC (Fisher Scientific BDB559864).

Validation

Laforin, GYS1, and PYGB antibodies were validated using knockout and/or knockdown cell lines and/or mouse tissues in previous studies (PMID: 34043942; PMID: 31353261; PMID: 31523006). anti-mouse-Sca1-APCCy7, anti-mouse-EpCAM-PECy7, anti-mouse-CD31-APC, anti-mouse-CD45-APC were validated through positive isolations of BASC and AT2 cells from the lung during FACS sorting in previouse studies(PMID: 36525966;PMID: 34622577).

Eukaryotic cell lines

Policy information about cell lines and Sex and Gender in Research

Cell line source(s)

A549 cells were purchased from ATCC.

Authentication

A549 line was freshly purchased from ATCC for this study, therefore, Lines were authenticated by ATCC

Mycoplasma contamination

Mycoplasma was not detected by ATCC, as well as periodic testing by our laboratory.

Commonly misidentified lines
(See ICLAC register)

n/a

Animals and other research organisms

Policy information about studies involving animals; ARRIVE guidelines recommended for reporting animal research, and Sex and Gender in Research

Laboratory animals

- Kras(LSL-G 12D)/p53(fl/fl)

- Kras(LSL-G 12D)/p53(fl/fl)/LKO(-/-)

- Kras(LSL-G 12D)/p53(fl/fl)/Gysfl/fl

All Animals were induced around 10-12 weeks old.

Wild animals

no wild animals were used in the study.

Reporting on sex

For all experiments, mixture of male and female mice were used. Sex-based analysis was not performed as it was not within the scope of the current study no previouse sex-differences were identified in this strain of mouse model of lung cancer.

Field-collected samples

no field collected samples were used in the study.

Ethics oversight

All animal studies were completed under the guidance of University of Kentucky (UK)and university of florida (UF) Institutional Animal Care and Use Committee (IACUC) and UK /UF Department of Laboratory Animal Resources (OLAR).

Note that full information on the approval of the study protocol must also be provided in the manuscript.

Clinical data

Policy information about clinical studies

All manuscripts should comply with the ICMJE guidelines for publication of clinical research and a completed CONSORT checklist must be included with all submissions.

Clinical trial registration	This study did not involve a clinical trial.
Study protocol	This study did not involve a clinical trial.
Data collection	This study did not involve a clinical trial.
Outcomes	This study did not involve a clinical trial.

Plants

Seed stocks	This study did not involve plant research.
Novel plant genotypes	This study did not involve plant research.
Authentication	This study did not involve plant research.